

Heavy pnictogens-based perovskite-inspired materials: Sustainable light-harvesters for indoor photovoltaics

Original

Heavy pnictogens-based perovskite-inspired materials: Sustainable light-harvesters for indoor photovoltaics / Schmitz, Fabian; Bhatia, Ribhu; Lamberti, Francesco; Meloni, Simone; Gatti, Teresa. - In: APL ENERGY. - ISSN 2770-9000. - 1:2(2023). [10.1063/5.0161023]

Availability:

This version is available at: 11583/2982542 since: 2023-09-28T09:26:28Z

Publisher:

AIP

Published

DOI:10.1063/5.0161023

Terms of use:

This article is made available under terms and conditions as specified in the corresponding bibliographic description in the repository

Publisher copyright

(Article begins on next page)

REVIEW ARTICLE | AUGUST 31 2023

Heavy pnictogens-based perovskite-inspired materials: Sustainable light-harvesters for indoor photovoltaics

Fabian Schmitz ; Ribhu Bhatia ; Francesco Lamberti ; Simone Meloni ; Teresa Gatti  

APL Energy 1, 021502 (2023)

<https://doi.org/10.1063/5.0161023>View
OnlineExport
Citation

CrossMark

Articles You May Be Interested In

Thermoelectric properties of pnictogen-substituted skutterudites with alkaline-earth fillers using first-principles calculations

J. Appl. Phys. (May 2016)

Enhanced interfacial thermal transport in pnictogen tellurides metallized with a lead-free solder alloy

Journal of Vacuum Science & Technology A (November 2015)

Electronic structure and thermoelectric properties of pnictogen-substituted $\text{ASn}_{1.5}\text{Te}_{1.5}$ ($A = \text{Co}, \text{Rh}, \text{Ir}$) skutterudites

J. Appl. Phys. (July 2015)

Heavy pnictogens-based perovskite-inspired materials: Sustainable light-harvesters for indoor photovoltaics

Cite as: APL Energy 1, 021502 (2023); doi: [10.1063/5.0161023](https://doi.org/10.1063/5.0161023)

Submitted: 7 June 2023 • Accepted: 11 August 2023 •

Published Online: 31 August 2023



Fabian Schmitz,¹  Ribhu Bhatia,²  Francesco Lamberti,³  Simone Meloni,^{2,a)}  and Teresa Gatti^{1,4,b)} 

AFFILIATIONS

¹Center for Materials Research, Justus Liebig University, Heinrich-Buff-Ring 17, 35392 Giessen, Germany

²Department of Chemical and Pharmaceutical Sciences, Università di Ferrara, Via Luigi Borsari 46, I-44121 Ferrara, Italy

³Department of Chemical Sciences, University of Padova, via Marzolo 1, 35131 Padova, Italy

⁴Department of Applied Science and Technology, Politecnico di Torino, C.so Duca degli Abruzzi 24, 10129 Torino, Italy

^{a)}E-mail: simone.meloni@unife.it

^{b)}Author to whom correspondence should be addressed: teresa.gatti@polito.it

ABSTRACT

The need for self-powered electronics is progressively growing in parallel with the flourishing of the Internet of Things (IoT). Although batteries are dominating as powering devices, other small systems, such as piezoelectric, thermoelectric, and photovoltaic systems, are attracting attention. These last ones can be adapted from their classical outdoor configuration to work preferentially under indoor illumination, i.e., by harvesting the spectrum emitted by LEDs and/or fluorescent lamps. However, crystalline silicon, the classical photovoltaic material for solar panels, has a bandgap not suitable for ensuring good efficiency with such spectra. With wider bandgaps, other semiconductors can come into play for this task. Still, the materials of choice, having to be integrated within households, should also satisfy the criterion of non-toxicity and maintain low-cost production. While lead-based halide perovskites cannot represent a valuable solution for this scope, due to the strong environmental and health concerns associated with the presence of Pb, analogous compounds based on the heaviest pnictogens, i.e., bismuth and antimony, could work as sustainable light-harvesters for indoor photovoltaic devices. In this Review, we focus on reporting the most recent developments of three compounds of this class: The double perovskite $\text{Cs}_2\text{AgBiBr}_6$ is first chosen as a model system for the other two, which are emerging perovskite-inspired materials, namely, $\text{Cs}_3\text{Sb}_2\text{I}_{9-x}\text{Cl}_x$ and bismuth oxyiodide. We show the potential of these semiconductors to play a crucial role in the future market of self-powering IoT devices, which will become a large class of devices in the electronics industry in the upcoming years.

© 2023 Author(s). All article content, except where otherwise noted, is licensed under a Creative Commons Attribution (CC BY) license (<http://creativecommons.org/licenses/by/4.0/>). <https://doi.org/10.1063/5.0161023>

I. INTRODUCTION

The development of the Internet of Things (IoT) is booming as the number of interconnected smart devices implemented in health-care,¹ buildings,² factories,³ vehicles,⁴ cities,⁵ and a plethora of other areas is continuously increasing. While in 2022 around 13×10^9 smart devices were estimated to exist, prognoses show that this number will more than double by 2030, with an expected amount of 30×10^9 smart devices connected to the IoT. Powering such an enormous number of remote devices is a crucial aspect since the usage of batteries poses several challenges, e.g., regular check

of their power levels requiring maintenance, thus increasing their operational costs. As many IoT devices find a use for indoor applications, indoor photovoltaics (IPVs) (i.e., solar cells that harvest light emitted from white light LED—WLED—or fluorescent lamps—FL-illumination) offer a possibility to continuously supply those devices with power when indoor light (and also diffuse light from the external environment) is on.⁶ Outdoor photovoltaics (OPVs) harvest the solar spectrum, which is reduced by atmospheric absorption losses and therefore subject to the Shockley–Queisser (SQ) limit that postulates a bandgap of 1.34 eV for an optimum power conversion efficiency (PCE) of around 33%, as depicted in Fig. 1.⁷ In contrast,

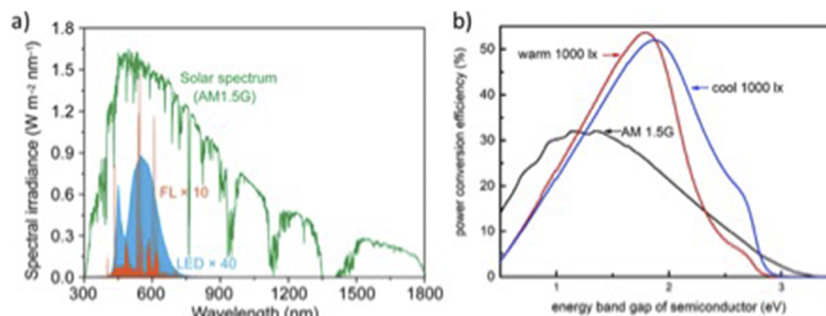


FIG. 1. (a) Comparison of WLED, FL, and AM 1.5G solar spectrum. (b) Dependence between light-harvester's bandgap and maximum achievable PCE for solar and WLED spectra. Reproduced with permission from Jarosz, Marczyński, and Signerski, *Mater. Sci. Semicond. Process.* **107**, 104812 (2020). Copyright 2020 Elsevier.

single-junction IPVs can exhibit a calculated maximum PCE of ~51%–68% for bandgaps between around 1.7 and 2 eV due to the vastly different emission spectra of WLEDs and FLs in comparison to the sun spectrum (Fig. 1).^{8–11} The discrepancy of those values originates from the nonuniformity of indoor light sources, e.g., whether they are calculated for warm or cold LEDs.¹⁰ Still, this shows that IPVs are not only able to surpass PCEs of OPVs but also that IPV solar absorbers need to possess much larger bandgaps to achieve such efficiencies. Additionally, indoor light sources provide light intensities of around 200 lux for living room environments and up to around 1000–2000 lux for bright light environments, e.g., office spaces or stores, in which IPVs are irradiated by a power density of around $0.5\text{--}3 \text{ W/m}^2$.^{9,12,13} This power density is four orders of magnitude lower than for typical working conditions of OPVs (1000 W/m^2). For example, the PCE of crystalline silicon solar cells drastically decreases when they are operated, not under outdoor but, under indoor conditions due to the silicon bandgap of 1.1 eV and increased Shockley–Read–Hall recombination at low power irradiation.^{14,15}

An alternative but promising class of light-harvesting materials to silicon are metal-halide perovskites (MHPs) owing to their advantageous optoelectronic properties, such as high charge carrier mobilities,¹⁶ long charge carrier diffusion lengths,¹⁷ high defect tolerance, low exciton binding energy,¹⁸ and high absorption coefficients, that enable the use of device film thicknesses below $1 \mu\text{m}$. When they are utilized as OPVs, perovskite photovoltaics (PPVs) reach competing PCEs to silicon solar cells.¹⁹ Classical MHPs possess the stoichiometry ABX_3 , where the A-site is occupied by an organic or inorganic monovalent cation like methylammonium (MA), formamidinium (FA), or Cs^+ , the B-site is occupied by Pb^{2+} , and X is a halide (I^- , Br^- or Cl^-). What contrasts these materials from many other semiconductors and makes them particularly suitable for IPVs is that their bandgap can be adjusted by halide tuning, i.e., the bandgap increases with decreasing anion size from iodide to chloride.^{20–22} This bandgap versatility in MHP materials made it possible for indoor perovskite photovoltaics (IPPVs) to surpass the 30% and rarely even the 40% PCE threshold.^{23–27} For example, the authors of the work of Dong *et al.* fabricated an IPPV with an indoor efficiency of 40.24% under 1000 lux FL illumination by modifying a perovskite layer with the botanic antioxidant tomato lycopene, which additionally protected the thin films against

oxygen and humidity and therefore increased their stability.²⁵ Moreover, the authors of the work of He *et al.* were able to achieve 40.1% indoor efficiency for $\sim 3 \text{ W/m}^2$ WLED (2700 K) irradiation by incorporating guanidinium into their perovskite and additionally passivating the perovskite's surface with 2-(4-methoxyphenyl)ethylamine hydrobromide to reduce nonradiative recombination.²⁷

Another favorable feature of PPVs is their solution-processability at low temperatures, which not only suppresses their processing costs but also enables the fabrication of flexible substrates.^{28,29} The latter can either be a practical necessity for many IoT devices or serve as an opportunity to realize creative designs.³⁰ However, PPVs tend to degrade under the influence of high temperatures, under ultraviolet light, and when they are in contact with water or oxygen, thus, in a humid atmosphere.^{31–33} This instability of PPVs usually causes a significant decrease in the initial PCE after several days or a few weeks, which is why often perovskite films are shielded from moisture and oxygen by protective interface layers or entire devices are encapsulated to increase their lifetimes to several weeks or even few months.^{25,34} It is important to note that stability tests for PPVs are usually performed under harsh conditions to simulate their usage as OPVs. Since indoor conditions are much gentler, e.g., involve lower working temperatures and UV irradiation, IPPVs will have enhanced device lifetimes in comparison to OPVs. Still, a requirement to reliably power IoT devices is that IPPVs sustain their PCE during their entire life cycles. This allows one to limit operational costs to control the charge level of batteries, guaranteeing IoT operatively in the dark hours, and manual replacement, if discharged. Furthermore, high-efficiency PPVs contain lead, which displays toxicity to the human body on exposure, hence representing a serious hazard for users in case of leakage, especially for use in any indoor IoT as well as in wearable devices.³⁵ Apart from exposition issues, the lead content also introduces questions and challenges regarding the end of life or recycling of such devices.³⁵

As a result, there is a broad variety of materials in which lead has been substituted by less toxic elements to exploit the structure's favorable properties while reducing their toxicity.³⁸ Of all lead-free perovskite materials, tin-based PPVs show the highest efficiencies but still suffer from low stabilities due to the hardly suppressible oxidation of Sn^{2+} to Sn^{4+} in ambient atmosphere because of its very low redox potential of 0.15 V.^{39,40} As a consequence, additional focus

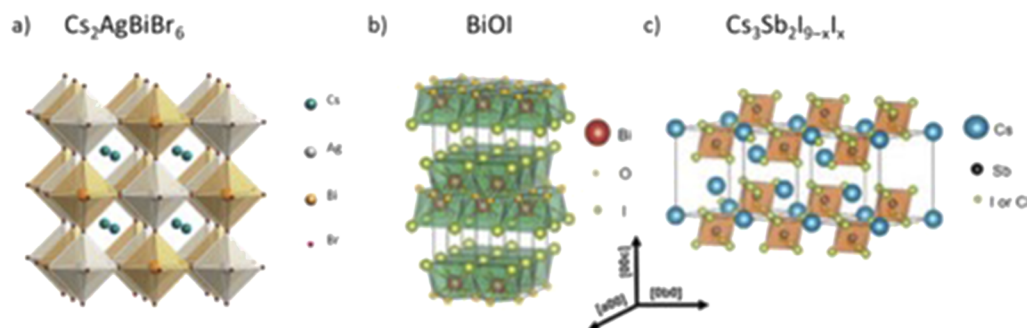


FIG. 2. Structures of the three heavy pnictogen-based perovskite and PIMs discussed in this review: (a) $\text{Cs}_2\text{AgBiBr}_6$ [reproduced with permission from Slavney *et al.*, J. Am. Chem. Soc. **138**(7), 2138–2141 (2016). Copyright 2016 American Chemical Society], (b) BiOI, and (c) $\text{Cs}_3\text{Sb}_2\text{I}_{9-x}\text{Cl}_x$ [Reproduced with permission from Peng *et al.*, Adv. Energy Mater. **11**(1), 2002761 (2021). Copyright 2021 Wiley].

had been set on the investigation of more stable lead-free perovskite materials. One of the earliest, and therefore also one of the most frequently explored materials, is the inorganic double perovskite (DP) $\text{Cs}_2\text{AgBiBr}_6$, whose structure is depicted in Fig. 2(a). In the following chapters, a general overview of its semiconducting properties, as well as a detailed summary of the most recent photovoltaic (PV) research, is given. However, due to its sub-optimal optoelectronic properties, as well as the issue of scarcity regarding the incorporated Ag, interest broadened toward other materials that no longer possess the perovskite structure but are still closely related to it, to benefit from its advantageous optoelectronic properties. Such materials are classified as perovskite-inspired materials (PIMs). There has been a special interest in materials based on heavy-pnictogen cations such as Bi^{3+} and Sb^{3+} in the form of halides or oxyhalides, e.g., bismuth oxyiodide (BiOI) and $\text{Cs}_3\text{Sb}_2\text{I}_{9-x}\text{Cl}_x$, depicted in Figs. 2(b) and 2(c),³⁷ that possess a similar electronic structure as Pb^{2+} . A crucial feature of lead-halide perovskites is the antibonding valence band maximum (VBM), originating from the $\text{Pb}(6s)-\text{X}(np)$ antibonding hybridization, while the conduction band minimum (CBM) is attributed to bond-like hybridization among $\text{Pb}(6p)$ orbitals, though there is no actual consensus in the literature on this latter point. Thus, the formation of some of the most energetically favorable defects, e.g., such as halide or lead vacancies, characterized by dangling bonds of the

complementary element forming the inorganic framework, results in states located deeply in the VB or CB.

It can be observed that, for the example of MAPbI_3 , the Pb 5p state is located close to the CBM. Therefore, Pb antisite defects, besides other intrinsic defects such as iodide vacancies, will be created either inside of the CB or slightly below the CBM, the so-called “shallow defects” [see Fig. 3(b)].^{41–44} As a result, electrons trapped in such defects require only low energy, close to or below the thermal energy at room temperature (≈ 25 meV), to overcome the energy barrier between the shallow trap and CBM (charge transition level) to be released. The formation of shallow hole defects works analogously, due to the energetic proximity between VBM and I 5p states, as depicted in Fig. 3(b).⁴⁴ Thus, charge carriers in trap states are likely to be released into the respective bands, which is why such materials are described as defect tolerant.

In contrast, binary II–VI, III–V, or group IV semiconductors tend to form a bonding VBM and an antibonding CBM that lead to the formation of trap states lying deep inside of the bandgap [Fig. 3(a)]. This leads to the formation of defect states deep within the bandgap. Accordingly, charge carriers trapped in such deep defect states require large energies, far above the thermal energy at room temperature, to be released back into the respective bands. Therefore, nonradiative recombination is far more likely to take

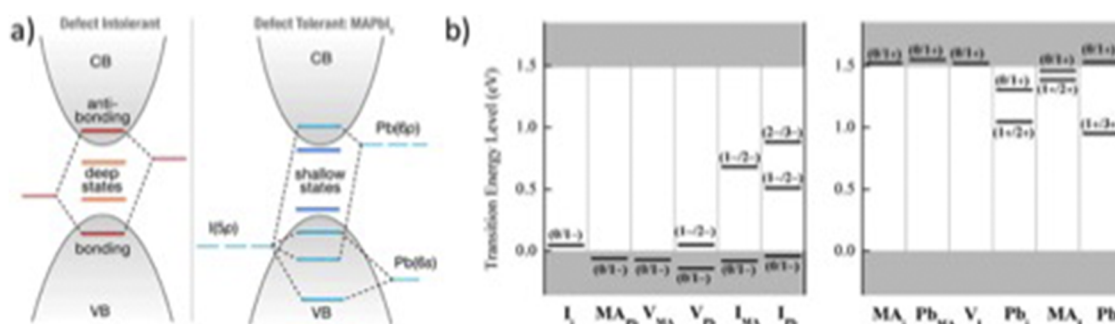


FIG. 3. (a) Electronic structure comparison of typical binary semiconductors (left) and a lead iodide perovskite (right). Reproduced with permission from Brandt *et al.*, Chem. Mater. **29**(11), 4667–4674 (2017). Copyright 2017 American Chemical Society. (b) Depiction of transition energy levels of point defects. Left: Intrinsic acceptors. Right: Intrinsic donors. Reproduced with permission from Yin, Shi, and Yan, Appl. Phys. Lett. **104**(6), 063903 (2014). Copyright 2014 AIP Publishing LLC.

place for charge carriers trapped in deep defect states than in shallow defect states.^{41,42} It is important to note that, even though there is a close structural relation between lead-halide perovskites (LHPs) and PIMs, the described formation of the electronic structure of the former cannot be fully transferred to the latter. For example, the degree of order of $[\text{BiBr}_6]^{3-}$ and $[\text{AgBr}_6]^{5-}$ octahedra in $\text{Cs}_2\text{AgBiBr}_6$ strongly affects its electronic band structure, which does not play any role for LHPs due to the presence of solely lead-halide octahedra in those materials. Moreover, the presence of Ag^+ as well as Bi^{3+} to substitute Pb^{2+} increases the number of intrinsic defect types and will be discussed further in Sec. II (Fig. 5). The electronic structures of all three PIMs of interest for this review are described in more detail in Sec. II.

High defect tolerance is a key factor in why materials possessing LHP-like electronic structures are well suited to be applied as IPV. Even at low-intensity indoor illumination, and therefore low concentrations of excited charge carriers, LHPs and PIMs achieve comparably high power conversion efficiencies due to the nature of shallow traps.^{27,45} Additionally, in those materials, defect concentrations can be reduced by passivating strategies and controlled crystal growth, as will be described in the following sections. This is an advantage over semiconductors like Si suffering from increased nonradiative recombination at low intensities due to the presence of deep trap states.

The double perovskite is here considered as a model compound in the field of heavy pnictogen-based lead-free PIMs and is further discussed in Sec. III to provide a general overview of the advantages and disadvantages of its use in IPV devices. The other two, BiOI and $\text{Cs}_3\text{Sb}_2\text{I}_{9-x}\text{Cl}_x$, are emerging species in the field, with high potential for use in low-cost, low-toxicity IPV. Overviews of recent research about BiOI are given in Sec. IV and about $\text{Cs}_3\text{Sb}_2\text{I}_{9-x}\text{Cl}_x$ in Sec. V.

Bi and Sb are elements from the 15th group of the periodic table, also known as group 5A, meaning that they share the same group as As, which is famous for its high toxicity in its pure form as well as in its compounds. They belong to the family of pnictogens as nitrogen (they are the “heaviest” ones in the group) and indeed this specific nomenclature refers to the suffocating action of pure N_2 gas (from ancient Greek: $\pi\upsilon\iota\gamma\omega$ “to choke” and $\gamma\epsilon\eta$, “generator”). Since the goal of applying Bi and Sb in IPV is the reduction of the biological hazard in case the devices get damaged and start to leak, an assessment of the toxicity of those elements is crucial. While the high toxicity of lead has been broadly investigated due to its vast utilization and abundance through the last several millennia, the biological hazards that stem from Sb and Bi exposition are far less explored. Bi is known to cause neurological dysfunction when humans are exposed to small doses periodically over a long time or large doses within a short time as it was observed for patients that ingested Bi-based medication.^{46–48} However, Bi has a toxic intake level of 15 g in comparison with a 1 mg toxic intake level for Pb for a 70 kg human.⁴⁹ This underlines the drastically reduced intoxication risk when Pb is substituted with Bi in IPV. In contrast to Bi, the toxic intake level of Sb is far lower (37 mg for a 70 kg human) but still more than an order of magnitude larger than that of Pb.⁵⁰ For details about the consequences of Sb intoxication, its potential carcinogenicity, and interferences with the metabolism of sugars and lipids, we refer the reader to recent literature reviews.^{51,52}

Apart from toxicity aspects, both Bi and Sb, unlike Pb, are included in the critical raw material (CRM) list of the European

Commission (Bi since 2017, Sb since its establishment in 2011). The CRM incorporates materials that are characterized by economic importance in industry and technology, are non-substitutable, and are characterized by a high supply risk. In comparison to the estimated ultimately available 20 000 Mt of lead, the scarcity of Sb and Bi is further underlined by their far lower estimated availabilities of 100 and 20 Mt, respectively.⁵³ Additionally, in 2016, 58% of the globally used lead was won from recycling,⁵⁴ while in 2021 these values were just 20% for Sb and 0% for Bi.⁵³ This drastically reduces the global warming potential (GWP) of lead (1.3 kg CO_2 -eq per kg) in contrast to Sb (12.9 CO_2 -eq per kg) and Bi (58.9 CO_2 -eq per kg).⁵⁴ Still, the potential global recycling rates for Sb and Bi are 55% and 48%, respectively, which could drastically decrease their GWP in the future.⁵³ Therefore, the route, in our opinion, is to find new experimental strategies for replacing both critical and toxic materials by using domestic (i.e., European) elements that would strongly diminish our dependence on imports.⁵⁵ For Bi, for instance (but the argument can be easily generalized to other critical materials), one must take into account that it is mainly extracted in Vietnam and China and the recycling processes are too complex and expensive.⁵⁶ This is of course only one part of the problem: At the early stages of life of IoT devices, as we are currently, the aim is to create a robust demand for these technologies and the only way to do so is to make them reliable by the realization of well-performing devices. The first steps in perovskites adoption for IPV started from the use of well-known toxic elements (such as lead, arsenide, and cadmium),⁵⁷ then research moved to attempt the implementation of a greener technology by resorting to atoxic but relatively scarce elements that can provide sufficient performance. In summary, the choice of a metal utilized in a light-harvesting material is a balancing act between its scarcity and performance and we cannot ignore this argument from the perspective of a more general and progressive advance in the field.

As the focus of this review lies specifically on recent advances in the research on MHPs and PIMs like $\text{Cs}_2\text{AgBiBr}_6$, BiOI , and $\text{Cs}_3\text{Sb}_2\text{I}_{9-x}\text{Cl}_x$ and their potential as indoor light-harvesting materials, for further information about other PIM-based IPV, we refer the readers to the reviews of Ünlü *et al.*⁵⁸ and Huang *et al.*,⁵⁹ providing more in-depth and complete overviews.

II. THEORETICAL BACKGROUND

Descriptors, like the nature (direct or indirect) of the electronic bandgap E_g , carrier mobilities and lifetimes, defect tolerance, absorption coefficient (α), the photoluminescence quantum efficiency (PLQE)(η), effective mass, static polaron binding energy, and Fröhlich electron–phonon coupling (EPC), are commonly used to identify material for photovoltaic applications. Density functional theory (DFT) has established itself as a powerful technique for first-principles investigations of solids for PV and optoelectronic devices, which can help establish the origin of these characteristics for pnictogens. Among the others, theoretical calculations and simulations have been performed on Sn-based perovskites, double perovskites, and other potentially defect-tolerant compounds ($\text{A}_3\text{B}_2\text{X}_9$, ABZ_2 , binary halides, and V–VI–VII materials), which have been identified as suitable alternatives to lead-based MHPs.⁵⁹

DPs are a promising class of materials of formula $\text{A}_2\text{B}'\text{B}''\text{X}_6$, with B' monovalent and B'' trivalent metal cations. $\text{A}_2\text{B}'\text{B}''\text{X}_6$ was

already considered in the early days of research on metal-halide perovskites for PV applications to eliminate Pb. Numerous combinations of A, B', B'', and X have been identified to be structurally and thermodynamically stable; however, **Cs₂AgBiBr₆ emerged as a reference system**. Cs₂AgBiBr₆ is appealing for its optoelectronic properties, 3D structure, long carrier lifetimes, and low carrier effective mass as LHPs and also higher stability and nontoxicity.

An important limitation of Cs₂AgBiBr₆ for OPVs is its relatively large bandgap, 2.18 eV. However, recently it was shown that this can be reduced by hydrogenation of the sample, achieving a record 1.64 eV low value.⁶⁰ This led to a corresponding high 6.37% power conversion efficiency. First-principles calculations revealed that the doping is interstitial, with three possible positions, denominated H₁(in), H₂(in), and H₃(in). This results in bonding states between H-1s and nearby cation orbitals. Depending on the interstitial site occupied by hydrogen atoms, one could obtain a wide [coupling between H₁(in)-1s, Br-4p and Ag-4d], narrow [coupling between H₂(in)-1s, Br-4p and Bi-6p], or a flat band [H₃(in)-1s and Br-4p] (see Fig. 4).

Additionally, device simulation of solar cells based on standard Cs₂AgBiBr₆ revealed that the optimization of the SnO₂/absorber interface can boost the cell's PCE to more than 14%.⁶¹ These findings suggest that the fundamental structural, optical, and electronic properties of Cs₂AgBiBr₆, on-purpose doping, which was not of great help in LHPs, and absorber/hole transport layer (HTL) interface must be better understood at an atomistic level to improve the efficiency of PIMs. In the following, we present a systematic review of theoretical results on the reference Cs₂AgBiBr₆ double perovskite. First, the structure–property relation and stability of Cs₂AgBiBr₆ are emphasized. Next, the fundamental optical and electronic properties, e.g., absorption and emission, followed by electron–phonon coupling and the effect of defects on the properties of the material are discussed.

Let us first focus on the relation between the Cs₂AgBiBr₆ structure and the fundamental optoelectronic properties of the material. At room temperature (RT), the stable crystalline phase of this double perovskite (lattice constant 11.7 Å) belongs to the Fm3m cubic space group.⁶² The ordered structure consists of alternating corner-sharing [AgBr₆]^{5−} and [BiBr₆]^{3−} octahedra forming a three-dimensional *checkboard*, with Cs⁺ being centered at the cavities. The corresponding Ag–Br/Bi–Br and Ag–Br–Bi bonds all maintain a 90° or 180° angle, and the bond length for Ag–Br and Bi–Br is comparable (2.804–2.828 Å). The shorter metal-halide distance to the corresponding lead-halide perovskite (3.18 Å) is an indication of the stronger B–X bonds at the basis of the improved stability of the Cs₂AgBiBr₆ framework.⁶³ However, there exists a relative mismatch between ionic radii (1.15 and 1.03 Å for Ag⁺ and Bi³⁺, respectively) and the electronegativity (1.93 and 2.02 for Ag⁺ and Bi³⁺, respectively) of the two metals. A consequence of such a mismatch is the volume variation and distortion/tilting of octahedra (mainly associated with bond lengths and bond angles) on exposure to external stimuli like temperature or pressure (mentioned later in this section). This has a significant effect on the electronic structure and consequently on the optoelectronic properties of the perovskites.⁶⁴

Concerning the electronic structure, Cs₂AgBiBr₆ VBM and CBM are very different from ordinary metal-halide perovskites. In this double perovskite, VBM and CBM are made of Ag-4d, Bi-6s, and Br-4p, and Ag-5s, Bi-6p, and Br-4s orbitals, respectively.^{65–67} VBM is

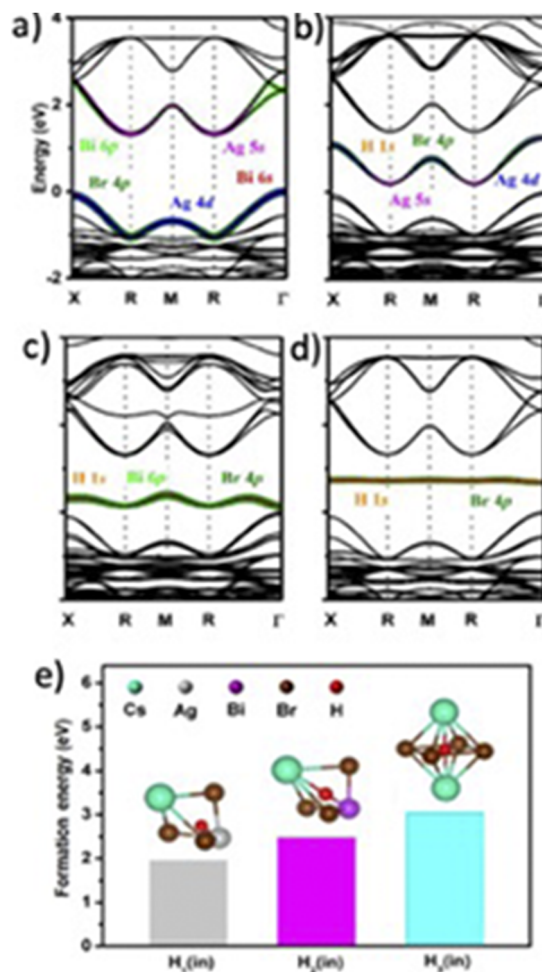


FIG. 4. (a) Band structure of a pure Cs₂AgBiBr₆ DP (host); (b)–(d) band structures of Cs₂AgBiBr₆ in the presence of hydrogen interstitial. Red, light green, blue, pink, dark green, and orange curves correspond to Bi 6s, Bi 6p, Ag 4d, Ag 5s, Br 4p, and H 1s orbitals, respectively; (e) H₁(in), H₂(in), H₃(in) represent different sites occupied by the interstitial hydrogen in the [AgBr₆]^{5−} and [BiBr₆]^{3−} octahedra, respectively. Reproduced with permission from Zhang *et al.*, Nat. Commun. 13(1), 3397 (2022). Copyright 2022 Author(s), licensed under a Creative Commons Attribution 4.0 License.

dominated by an antibonding hybridization between Ag-4d and Br-4p, with a minor contribution from antibonding Bi-6s and Br-4p. CBM mainly consists of a mixture of Bi-6p orbitals, Bi-6p and Br-4p antibonding states, and Ag-5s, Br-4p bonding states. At variance with ordinary halide perovskites, Cs₂AgBiBr₆ presents an indirect bandgap. The presence of [AgBr₆]^{5−} and [BiBr₆]^{3−} in the framework raises the question of whether in the Cs₂AgBiBr₆ structure, these octahedra are alternated or random. Octahedra order/disorder significantly affects the optoelectronic properties, including bandgaps, lattice distortion, defects, and carrier mobility, and can therefore be used to manipulate light absorption.

The first-principles calculation presented in the work of Yang *et al.* revealed enhanced light absorption in the visible and

near-infrared region on moving from an ordered, i.e., alternated $[\text{AgBr}_6]^{5-}$ and $[\text{BiBr}_6]^{3-}$ octahedral structure, to partially disordered to completely random ones, as depicted in Fig. 12(b). Depending on the degree of disorder, changes in the band structure from indirect to pseudodirect and band shrinkage by 1–1.5 eV were observed.⁶⁸ Unfortunately, calculations also revealed that such a random structure and the ensuing improved band structure were possible only if $\text{Cs}_2\text{AgBiBr}_6$ was synthesized by quenching from temperatures beyond 1200 K, which greatly limit practical applications. Exposing $\text{Cs}_2\text{AgBiBr}_6$ to high pressures appears to be another alternative to manipulate the material's properties. For instance, the authors of the work of Fu *et al.* computed the bandgap and structural evolution of the system for P values in the experimental range.⁶⁹ Consistent with their experimental findings, a decrease in the bandgap with increasing pressure in the 1 atm–12 GPa range is observed for the cubic phase. However, a more complex trend of bandgap evolution is observed for the tetragonal phase. In this case, the bandgap decreases from 2.84 to 2.74 eV in the 1 atm to 6 GPa pressure range, followed by an increase to 3.01 eV for pressures beyond 6 GPa. Furthermore, a semiconductor-to-metallic transition is reported at ~20 GPa in the work of Islam *et al.*⁷⁰ Such bandgap evolutions are attributed to the pressure-induced symmetry breaking of $[\text{AgBr}_6]^{5-}$ and $[\text{BiBr}_6]^{3-}$ octahedra. In other words, pressure induces tilting of octahedra, the soft mode in perovskites, leading to orbital interactions resulting in the evolution of the bandgap.

Let us now focus on the stability of $\text{Cs}_2\text{AgBiBr}_6$ and summarize theoretical results, shedding some light on its superior stability. Two parameters must be considered: (i) the tolerance factor—here we highlight the more accurate formulation recently proposed,

$$\tau = r_A/r_B - n_A \left(n_A - \frac{r_A}{r_B} \right) \ln \left(\frac{r_A}{r_B} \right)$$

with r_A , r_B , n_A being ionic radii and oxidation state of A and B ion, respectively, and (ii) the octahedral factor,

$$\mu = r_B/r_X,$$

where r_X is the ionic radius of the X ion. Both factors are commonly used to evaluate the structural stability of ABX_3 perovskites. Typically, a perovskite is structurally and thermodynamically stable when $\mu < 4.18$ and $0.44 \leq \tau \leq 0.9$, and both conditions are essentially met by $\text{Cs}_2\text{AgBiBr}_6$, which presents a $\tau = 0.56 - 0.60$ and a $\mu = 4.07 - 4.21$. The work of Chapa *et al.* provided evidence of mechanical stability of $\text{Cs}_2\text{AgBiBr}_6$ via DFT calculations, while the thermodynamic stability was confirmed by Zhang and co-workers.^{71,72} They evaluated the decomposition energies of possible decomposition pathways like CsBr, AgBr, Cs_2AgBr_3 , CsAgBr_2 , and $\text{Cs}_3\text{Bi}_2\text{Br}_9$ via first-principles calculations and all the values they obtained appear to be positive and higher than 20 meV, suggesting a high thermodynamic stability of $\text{Cs}_2\text{AgBiBr}_6$.

Concerning the properties of $\text{Cs}_2\text{AgBiBr}_6$ affecting its performance, the bandgap is certainly the most relevant intrinsic property for a light-harvesting material because a precise knowledge of E_g helps to predict the PV maximum efficiency under given illumination conditions, e.g., within the Shockley–Queisser (SQ) framework. Here, one assumes that all the incident light with energy

larger than E_g is absorbed. However, in real materials, there is a non-negligible transmission of photons with energies greater than the bandgap. $\text{Cs}_2\text{AgBiBr}_6$ has an indirect bandgap with reported values spanning a large energy range, from 1.95 to 2.25 eV.^{66,73} Within the SQ formalism, these values would allow for theoretical photocurrents and PCEs under AM 1.5G illumination conditions between 17 mA/cm² and a PCE of 25% for $E_g = 1.9$ eV, and 6 mA/cm² and a PCE of 12% for $E_g = 2.5$ eV. These values are very optimistic concerning the more realistic spectroscopic limited maximum efficiency (SLME) of 7.9%, estimated based on first-principles calculations, which consider the calculated shape of the absorption spectrum and nonradioactive recombination. This discrepancy suggests that a thorough theoretical analysis of the optical properties is needed when screening materials for PV applications.^{74,75}

A typical $\text{Cs}_2\text{AgBiBr}_6$ absorption spectrum can be seen in Fig. 5(a). There is high absorption below 340 nm (3.6 eV), a strong feature at around 440 nm (2.8 eV), and weak absorption at lower energy. The high absorption is attributed to the vertical transition, and the direct bandgap, while the strong feature observed in the spectra is still under debate; finally, the long tail toward low energies indicates the absorption due to the indirect bandgap. It should be noted that the sharp peak at 440 nm corresponding to 2.8 eV contributes more than 20% of the overall light absorption of $\text{Cs}_2\text{AgBiBr}_6$ perovskite. Peaks at high energies, which are of limited interest for OPVs, are very relevant for indoor applications, and understanding their origin may help optimize present materials or develop newer ones. Some speculations for the origin of the sharp peak include excitonic absorption, charge transfer-like transition between Ag and Bi/Br orbitals, or localized Bi 6s–6p transitions. Even though experimental investigations favor the latter to be the cause of this observed absorption peak, there is no theoretical evidence supporting this claim.⁷⁶

The photoluminescence (PL) yield of $\text{Cs}_2\text{AgBiBr}_6$ was reported to be in a very low range from 0.01% to 0.08% for an excitation density comparable to one sun, while the decay of the PL intensity is rather slow, indicating long-living charge carriers.⁷⁷ This strengthens the interest of the community as these characteristics are promising for efficient extraction of charge carriers. The PL spectrum is broad and shows a Stokes shift [Fig. 5(a)], which is also confirmed by Baranowski and co-workers, who reported a ~500 meV shift between PL and PLE spectra.⁷⁸ This Stokes shift is attributed to a strong electron–phonon coupling, a relevant phenomenon affecting PV cells' efficiency, discussed in detail below. This conjecture was confirmed by comparing phonon energies as obtained from Raman spectra with corresponding values obtained from DFT calculations.⁷⁸ Nevertheless, the origin of the PL emission is still debated. The work of Baranowski *et al.* provided evidence that the PL peak results from spatially localized color centers, which can be either intrinsic self-trapping of exciton/carriers or defects.⁷⁸

PL results are associated with mechanisms—electron–phonon coupling (EPC) and polaronic effects on carrier mobility—which critically affect the efficiency of $\text{Cs}_2\text{AgBiBr}_6$ -based PV devices. Let us focus first on the former phenomenon, EPC, i.e., the scattering of moving electrons by longitudinal optical (LO) phonons, when atoms move parallel to the phonon propagation direction, or transverse optical (TO) phonons when atoms move in the plane

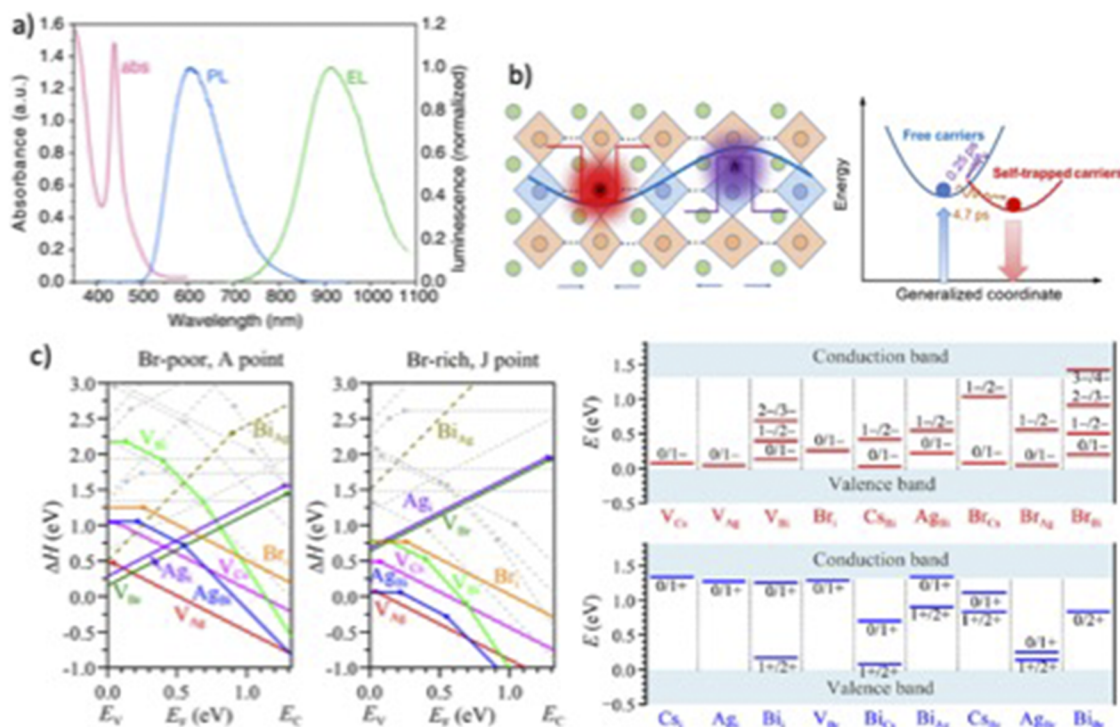


FIG. 5. Optical, transport, and defect properties of $\text{Cs}_2\text{AgBiBr}_6$. (a) Absorption and emission spectra of $\text{Cs}_2\text{AgBiBr}_6$ (here, abs stands for absorption, PL for photoluminescence, and EL for electroluminescence). Reproduced with permission from W. Tress and M. T. Sirtl, *Sol. RRL* **6**(2), 2100770 (2022). Copyright 2022 Author(s), licensed under a Creative Commons Attribution 4.0 License. (b), left: Schematic of the self-trapping mechanism of charge carriers by acoustic phonons or deformation potential. The dots between adjacent perovskite octahedra represent the lattice units omitted for the sake of simplicity. This panel shows that the deformation of the lattice results in a localizing potential for holes and electrons. This localizing potential controls the dynamics of charge carriers: Trapping and de-trapping of holes and electrons follows the dynamics of phonons responsible for the formation of the localizing potential wells. (b), right: Schematic of the energy diagram for carrier self-trapping. Free electrons in the conduction band are energetically driven to localizing potential, where they remain trapped. Reproduced with permission from Wu *et al.*, *Sci. Adv.* **7**(8), eabd3160 (2021). Copyright 2021 Author(s), licensed under a Creative Commons Attribution 4.0 License. (c), left: Point defect formation energies, ΔH (eV), of intrinsic defects in $\text{Cs}_2\text{AgBiBr}_6$ as a function of the Fermi level, E_F , at representative Br-rich and Br-poor conditions. Defects with very high ΔH values are shown by the dashed lines. (c), right: Calculated transition energy for intrinsic acceptors (top) and intrinsic donors (bottom). Reproduced with permission from Xiao *et al.*, *ChemSusChem* **9**(18), 2628–2633 (2016). Copyright 2016 Wiley.

orthogonal to their propagation direction. Broadly speaking, the carrier–optical phonon interactions affect the carrier’s mobility while the carrier–acoustic phonon interactions influence the thermal properties of materials, like thermal conductivity and thermal expansion coefficient. For instance, for halide perovskites, it has been pointed out that low thermal conductivity can lead to a temperature rise in an operating device and cause stability issues. The resulting large thermal expansion can give rise to thermal strain and stress,⁸¹ possibly mitigated by a self-protecting mechanism recently proposed.⁸²

On the other hand, perovskites are susceptible to local distortion by charge carriers leading to the formation of polarons. A polaron is a quasiparticle formed because of conduction electrons (or holes) interacting with their self-induced polarization in the polar semiconductor or ionic crystal. This is expected to be especially important in the case of soft and potentially polar systems, like ordinary and double perovskites. Polarons can be classified according to the degree of the spatial localization of the carrier. One distinguishes between small when it is localized within a single site, or large, when it involves several lattice sites, polarons.

Herz and co-workers showed that for traditional perovskites (like methyl ammonium lead iodide—MAPI—or formamidinium lead iodide—FAPI), at room temperature, charge carrier scattering is dominated by the coupling between carriers and longitudinal optical (LO) phonons rather than interaction with acoustic phonons or from ionized impurities.⁸³ Within the Fröhlich model (which addresses electrons in ionic crystals or polar semiconductors and considers the long-range interaction between an electron and a polar optical phonon mode under the continuum approximation), the strength of this carrier–LO phonon interactions is characterized by Fröhlich polaron coupling constant α , such that

$$\alpha = \frac{2\pi q^2}{h} \left(\frac{1}{\epsilon_{\text{inf}}} - \frac{1}{\epsilon_0} \right) \sqrt{\frac{\pi m^*}{h\omega_{\text{LO}}}},$$

where q is the elementary charge, h is the Planck constant, ϵ_{inf} and ϵ_0 are the dielectric constant at infinite and zero frequency, respectively, m^* is the effective mass of the electron or hole, and ω_{LO} is the frequency of the dominant phonon. For conventional ionic

inorganic semiconductors, the Fröhlich coupling constant is significantly smaller than unity, while the same adopts values of ~ 1 to 2 for electrons and holes in MAPbI₃, respectively. These values are considered to be “intermediate” for traditional halide perovskites,⁸⁴ giving rise to polarons that can limit charge carrier’s mobility in MAPbI₃.⁸⁵ However, first-principles calculations presented in the work of Steele *et al.* on Cs₂AgBiBr₆ revealed α_e and α_h values of 2.54 and 2.0 , respectively.⁸⁶ Similar values (2.68 and 2.52 for electrons and holes, respectively) have been reported in the work of Wu *et al.*⁷⁹ Using the Feynman–Osaka formula, the same group estimated polaron mobilities to be equal to ~ 27 (e) and 33 (h) cm²/s V for electrons (e) and holes (h), respectively. These values are much lower than those observed for selected LHPs, e.g., CH₃NH₃PbBr₃, showing mobilities of $\mu_e \sim 150$ (e) and $\mu_h \sim 79$ (h) cm²/s V⁻¹, while CsPbBr₃ shows mobilities of $\mu_e \sim 48$ and $\mu_h \sim 42$ cm²/s V⁻¹.¹⁸⁷ These results suggested that only Fröhlich coupling may not be responsible for such a large difference in carrier mobility between the Bi-based double perovskite and LHP. This prompted investigations on the role of the deformation potential: local lattice deformations produced by an electron/hole carrier induce changes in the band structure localizing it in a small polaron. When electron–phonon interaction strength is above a given threshold, a transition from free-carriers to a self-trapped state is observed.⁸⁸ Following Toyozawa, self-trapping by charge-induced deformation potential can be assessed by a factor, g , that in the case of cubic lattices reads

$$g = \Xi 2m / 6\hbar 2Ca, \quad (1)$$

where Ξ is the deformation potential, m is the bare electron effective mass, C is the elastic constant, and a is the lattice parameter.⁸⁹ For Cs₂AgBiBr₆, the authors of the work of Wu *et al.* reported values of 0.87 and 0.89 for electrons and holes, respectively.⁷⁹ Values very close to unity indicate the possibility of self-trapping of both charge carriers in small polarons with a coherent length comparable with the lattice parameter, ~ 11.2 Å. They speculate that both optical phonons (Fröhlich coupling) and acoustic phonons (deformation potential) synergistically contribute to the electron–phonon scattering mechanism in Cs₂AgBiBr₆. In other words, electron and hole carriers in Cs₂AgBiBr₆ are first localized by optical phonons and then self-trapped by acoustic phonons, which further localize the charge carriers [Fig. 5(b)].

Beyond electron–phonon coupling, which has proven to be an important aspect determining the transport properties in Cs₂AgBiBr₆, it is imperative to understand the role of defects, their stability, hence abundance according to thermodynamics, and their effect on the properties of materials at a fundamental level: This may allow achieving highly efficient optoelectronic devices. Concerning defects, one usually distinguishes between point defects (i.e., vacancies, interstitials, and antisites), line defects (i.e., dislocations), plane defects (i.e., surfaces and grain boundaries), and bulk defects (i.e., voids or precipitates). One of the reasons for the success of lead-based MHPs is their high defect tolerance, i.e., that the presence of defects does not result in deep defect states, defect-induced localized electronic states with energy close to the middle of the bandgap that, according to the Shockley–Read–Hall theory, induce nonradiative recombination [see Fig. 3(b)]. This defect tolerance is attributed to the strong antibonding coupling between Pb s and halide p orbitals for the VB, and Pb p and halide s ones

for the CB.⁹⁰ Cs₂AgBiBr₆ DP exhibits lower defect tolerance owing to the presence of two B-site metal ions. The authors of the work of Xiao *et al.* computed the formation enthalpies and thermodynamic transition energy levels of typical point defects (vacancies, cation-on-anion antisites, anion-on-cation antisites, and interstitial) in Cs₂AgBiBr₆ under representative Br-poor and Br-rich conditions [Fig. 5(c)].⁸⁰ They concluded that even in Ag-rich conditions, Ag vacancies are the most easily formed defects. Ag vacancies, however, are shallow and do not deteriorate optoelectronic performance, like Pb vacancies in MAPbI₃ (see Fig. 3). The dominant deep-level acceptor defects include Ag_{Bi}, Bi_{Ag} antisites, and V_{Bi}. They suggested that the formation of deep defects can be significantly suppressed by synthesizing the materials under a Br-poor/Bi-rich growth condition, which was deemed necessary for PV and other optoelectronic applications of Cs₂AgBiBr₆. Similar conclusions were reported in the work of Li *et al.*⁹¹ However, in addition to identifying Ag_{Bi}, Bi_{Ag} antisites, and V_{Bi}, the authors also identified halogen vacancy V_{Br} as a deep-level defect. It is worth remarking that defects seem to be very sensitive to the synthesis environment of Cs₂AgBiBr₆.

Though experimental works have identified some of the detrimental defects mentioned above and developed strategies to passivate them, the charge carrier trapping mechanism is unclear. Recently, the authors of the work of Liu *et al.* implemented machine learning methods, DFT calculations, and nonadiabatic molecular dynamics (NA-MD) to investigate the recombination mechanism in defective Cs₂AgBiBr₆ induced by negative V_{Br}.⁹² The distribution of excess charge between the metal atoms close to the vacancy was identified to be at the basis of the deep trap state. According to their calculations, the electrons from the vacancy are first localized on the adjacent (to the vacancy) Bi atom and then are shared with the neighboring Ag atom. This charge transfer transforms the trap state from shallow to deep. The same authors also proposed a strategy to mitigate this effect. Doping the system with indium, and replacing the Ag involved in the trap with In, prevents the delocalization of charge responsible for deep trapping (Fig. 6). The work of She *et al.* revealed another mechanism for the mitigation properties of indium: The longer In–Bi bond and the relatively weaker hybridization of the In- p and Bi- p orbitals prevent the formation of deep traps.⁹³

We conclude this part on Cs₂AgBiBr₆ mentioning that, so far, investigation of trapping and recombination at surfaces and grain boundaries in this material is still lacking. It is worth remarking that in the case of LHPs, it was shown that often trapping and recombination of charge carriers occurs at grain boundaries and surfaces⁹⁴ and more specifically interfaces between the perovskite and (HTL)/electron transport layer (ETL). Hence, theoretical research on these extended defects is especially important for progress of the field.

Bismuth oxyiodide (BiOI), a PIM composed of elements from the V, VI, and VII groups has recently gained popularity as a potential candidate for PV thanks to its 10^4 cm⁻¹ absorption coefficients in the visible wavelength range.⁵⁹ BiOI, belonging to a tetragonal structure with space group $P4/nmm$, is composed of a layer of (Bi₂O₂)²⁺ slabs interleaved by a double layer of I, forming –I–Bi–O–O–Bi–I– slabs stacked along the c -axis held together by nonbonding van der Waals interactions [Fig. 7(a)]. As a result of such a structural configuration, an electric field is developed between the (Bi₂O₂)²⁺ and

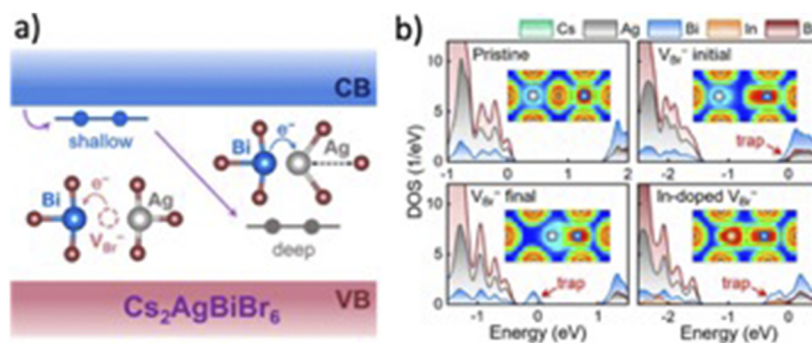


FIG. 6. (a) Mechanism of sharing of the electrons trapped in a bromide vacancy. The electron is initially accepted in a Bi orbital and then shared with Ag. This brings to a sizable and local distortion of the lattice transforming the shallow into a deep trap state. (b) Element-projected density of states (DOSs) in pristine and In-doped Cs₂AgBiBr₆. The insets show the electron localization function (ELF) maps around the vacancy sites. Red and blue indicate ELF values of 1 and 0, respectively. This panel shows that indium prevents the formation of deep trap states. Reproduced with permission from Liu *et al.*, J. Phys. Chem. Lett. **13**(16), 3645–3651 (2022). Copyright 2022 American Chemical Society.

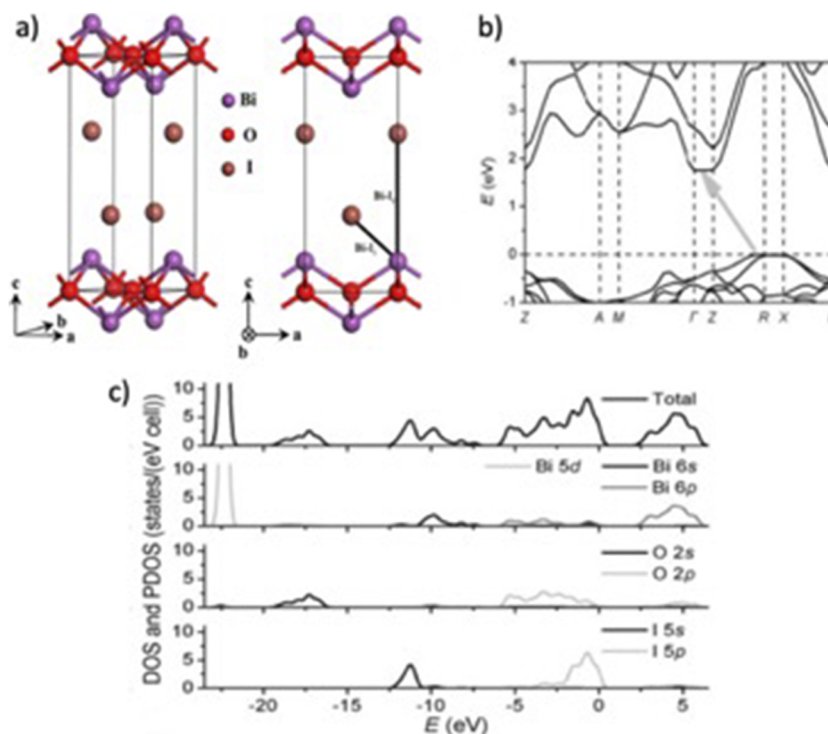


FIG. 7. (a) Crystal structure of BiOI. BiOI is a 2D material made of BiO layers intercalated by I ions. (b) BiOI band structure. The arrow highlights the indirect nature of the bandgap. (c) Total density of states (DOS) and individual atomic contributions to it (PDOS) of BiOI. This shows that the valence band maximum mostly comes from I 5s and 5p orbitals, while the conduction band minimum mostly arises from Bi 5s and 6d. Reproduced with permission from W. L. Huang and Q. Zhu, Comput. Mater. Sci. **43**(4), 1101–1108 (2008). Copyright 2008 Elsevier.

two I⁻ layers. A prior research, assessing the performance of BiOI as a photocatalyst, reported improved photocatalytic activity due to effective electron–hole charge carrier separation by this built-in electric field.⁹⁵ This mechanism of charge separations is appealing also for PV applications, but, no reported theoretical studies have

explored the influence⁹⁶ of this intrinsic property on charge carrier dynamics in BiOI for PV applications. Furthermore, like other heavy pnicogens-based semiconductors, an important limitation of BiOI for OPV is its wide indirect bandgap of ≈ 2 eV [Fig. 7(b)]. While the indirect nature is still a problem for IPV, its relatively large bandgap

value is optimal for indoor light harvesting owing to the spectra of indoor light sources being blue-shifted compared to the AM 1.5G spectrum, as shown in Fig. 1.³⁷

It is useful to analyze the electronic structure of BiOI in comparison with that of lead-based perovskites, where the valence 6s orbitals of Pb^{2+} hybridize with the halide p orbitals to form a pair of bonding and antibonding states within the upper VB. The empty valence Pb p orbitals also hybridize with the anion s orbitals to form the antibonding state at the CBM. In addition, the high spin-orbit coupling results in a further decrease in bandgap.⁸⁴ The combination of these effects is at the basis of the formation of only/predominantly shallow trap states in lead-halide perovskites, a key characteristic for high PV performance materials (see Sec. I for more details). BiOI shares several characteristics with the electronic structure of these last ones, as band edges are predicted to have an antibonding orbital character. In particular, the VBM is predominantly made of I-5p orbitals hybridizing with Bi-6s ones with some contribution from O-2p states. The CBM is mainly made of Bi-6s, with contributions from s and p orbitals of I and O [Fig. 7(c)]. This raises hope that BiOI is defect tolerant.

One of the first relevant computational and experimental works on BiOI has indeed found that the material is tolerant to vacancy and antisite defects. To understand the tolerance of BiOI to intrinsic point defects, the authors of the work of Hoye *et al.* calculated the formation energy as a function of Fermi energy of V_{Bi} , V_{O} , and V_{I} vacancies, and O_{Bi} , I_{O} , Bi_{O} , Bi_{I} , O_{Bi} , I_{Bi} antisite defects.⁹⁷ The authors concluded that owing to their low formation energies, V_{Bi} , O_{Bi} , and V_{I} were the prevalent defects under I-rich conditions, while V_{I} and O_{I} prevail under Bi-rich conditions (Fig. 8). Other defects had significantly higher formation energies ($\Delta H_{\text{D,q}} > 1$ eV), implying that they had much lower equilibrium concentrations and can likely be neglected. It should be noted that all the defects were shallow because their charge transition levels were either inside or close to the band edges. They also reported a high (relative) dielectric constant of 45, which typically means effective screening of charged defects, consequently leading to a low trapping probability. This provides the theoretical rationale for the defect tolerance of BiOI.

These conclusions were challenged by the authors of the work of Brandt *et al.*, who investigated the decay time of charge carriers in a series of materials, including BiOI and SbSeI pnictogens, by time-resolved PL (TRPL).⁴¹ They found that the carrier lifetimes of explored pnictogens were hundreds of nanoseconds shorter with respect to carrier lifetimes observed in $\text{CH}_3\text{NH}_3\text{PbI}_3$. These results suggest defect tolerance as assessed by thermodynamic transition energy level may be an insufficient heuristic to judge the suitability of a material for PV applications. Additionally, photoinduced current transient spectroscopy measurements performed in the work of Huq *et al.*⁹⁸ showed that BiOI films have deep traps located at 0.3 and 0.6 eV from the band edges, which were not identified in the calculations.

The authors of the work of Ganose *et al.*⁴³ remarked on the defect tolerance challenge in wider bandgap semiconductors. Here, we report some criteria that have been proposed in the literature and that theoretical research may in screening to help address the defect tolerance challenge in wider bandgap semiconductors. The authors of the work of Ganose *et al.* proposed enhancing ionic (vibrational) contributions to the static dielectric constant, exploiting, for

example, spontaneous electric polarization, like in SbSI possessing a Curie temperature of 291 K, or flexibility of the framework, like in MHPs. Therefore, the authors of the work of Brandt *et al.*⁴¹ themselves proposed additional screening criteria for the selection of materials that are likely to exhibit a long carrier lifetime. The first criterion stems from the heuristic observation that there is a correlation between the symmetry of the crystal structure's low effective masses and long lifetimes (>660 ns), such as double perovskite $\text{Cs}_2\text{AgBiBr}_6$, among the materials considered here. The second criterion is the importance of the choice of anion for a given cation. As already mentioned in the Introduction, one of the reasons for the defect tolerance of MHPs is the formation of antibonding orbitals at the valence band edge. The conclusion of the work of Brandt *et al.* is that the energy mismatch between Bi(6s) and I(5p) orbitals makes their hybridization insufficient to achieve good defect tolerance.

A comment is in order about theoretical research on defects and related electronic states. The apparent mismatch between calculations, which reveal no likely defects associated with such deep gap states, and experimental results from the work of Brandt *et al.* and, especially, that of Huq *et al.* can be due to several facts. First, defect calculations are typically performed in the zero-temperature approximation, i.e., after creating the defect, the atomistic structure of the sample is either held fixed at the perfect crystalline structure or relaxed to the nearest local minimum. A limited number of studies, mostly devoted to lead-based MHPs, have shown that the finite temperature structure of the defect can significantly differ from the one obtained within the standard zero-temperature approximation.^{99,100} Moreover, at finite temperature, the structure can significantly change from charge state to charge state, a phenomenon strongly affecting the nature of defect states that is overlooked in the zero-temperature approximation. The mismatch between computational results and that presented in the work of Huq *et al.* is not necessarily due to artifacts resulting from the simulation protocol but might also be due to processes that have not been investigated, so far. For example, for LHPs, on which research has been more intense, it was found that interstitial iodide, a shallow defect in the bulk, may become a trap state at grain boundaries.⁹⁴ Finally, the analysis of shallow or deep gap states focuses on the equilibrium abundance of defects. This, however, disregards nonequilibrium effects, i.e., defect abundance beyond their thermodynamic value: Once formed during film deposition, typically a nonequilibrium process, annihilation might be too slow for defect concentration to achieve its equilibrium value, possibly resulting in the observed deep gap state. Thus, despite the significant progress made in this field, systematic theoretical research is needed to address defect tolerance in BiOI, which might also help identify heuristic criteria for selecting novel PV materials.

The search for lead-free PIM alternatives has focused on elements with electronic configurations analogous to lead in LHPs as well as a crystal structure based on corner-sharing $[\text{PbX}_6]^{4-}$ octahedra. Indeed, the defect tolerance of the latter has been linked to the high symmetry of these structures and the ionic-covalent bonding arising from the stable ns^2 configuration of the Pb^{2+} cations hybridizing with halide anions.⁹⁰ Both antimony and bismuth formally fit this criterion as their valence ns^2 electrons hybridize with halide anion orbitals to form a similar electronic structure. Antimony-based compounds are more appealing due to their

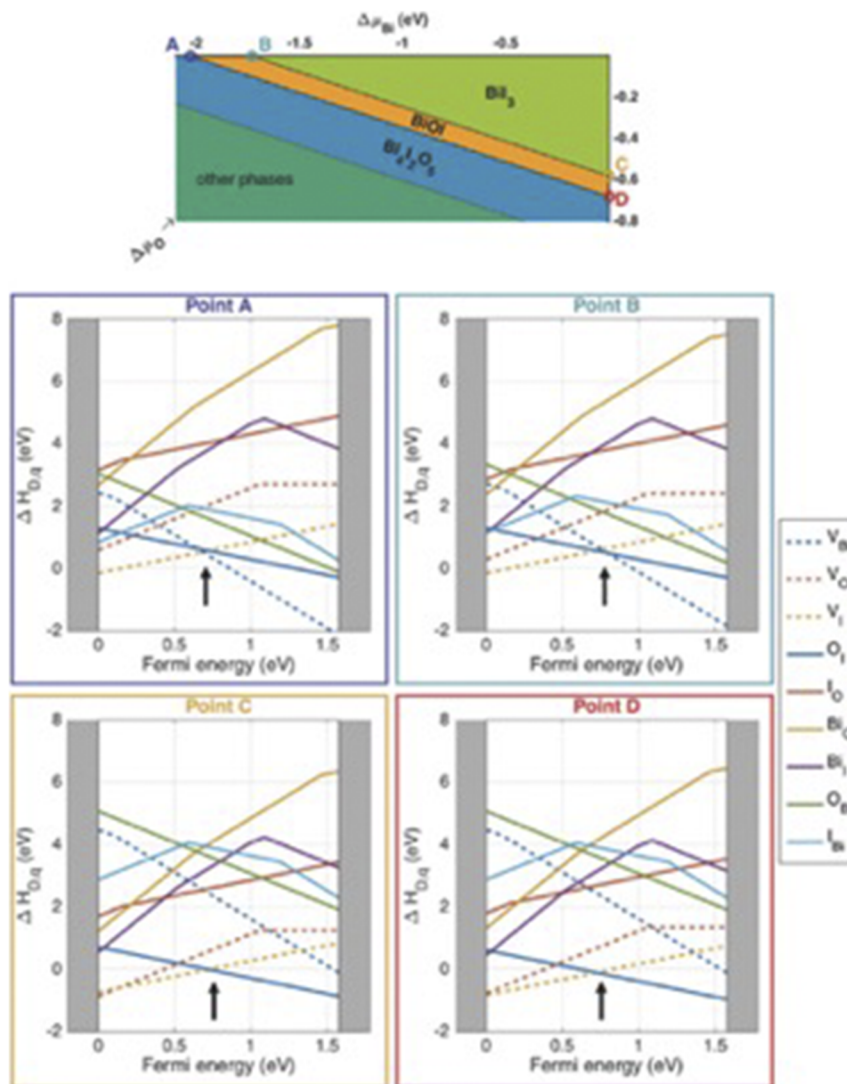


FIG. 8. Top: Phase diagram of the Bi–O–I system, showing the stability region of BiOI as well as phases with close equilibrium conditions. Bottom: Formation energy of intrinsic point defects in BiOI at the four extremes in the phase-stable region for BiOI. These diagrams allow one to identify the most likely defects in the various thermodynamic conditions as a function of the fermi energy of the system. Points A and B correspond to I-rich growth conditions, whereas points C and D correspond to Bi-rich conditions. Adapted with permission from Hoyer *et al.*, *Adv. Mater.* **29**(36), 1702176 (2017). Copyright 2017 Author(s), licensed under a Creative Commons Attribution 4.0 License.

appreciably smaller exciton binding energy (~ 100 meV range) compared to the bismuth-based counterparts (~ 300 to 400 meV), promising a higher PCE.¹⁰¹ However, due to the +3-oxidation state of Sb, it is not possible to directly substitute it in ABX_3 materials. Instead, a defect-ordered $\text{A}_3\text{B}_2\text{X}_9$ perovskite can be formed, with A^+ : MA^+ , FA^+ , Rb^+ , K^+ , Cs^+ ; B^{3+} : Sb^{3+} ; X^- : Cl^- , Br^- , I^- . This can be thought of as $\text{A}_3\text{B}_2(\cdot)\text{X}_9$, in which every third metal cation in ABX_3 is substituted for a vacancy, (\cdot). Systems with $\text{A}_3\text{B}_2\text{X}_9$ composition can arrange in the structure of a different kind and often form 0D materials of the kind shown in Fig. 9(a), consisting of isolated biocahedral $[\text{B}_2\text{X}_9]^{3-}$ groups alternating with A^+ -site cations.

The band structure of such systems is rather flat, implying high effective masses of charge carriers, hence reduced mobility and limited efficiency.⁸⁴ However, this effective mass can be reduced by tuning the A-site or X-site ions to stabilize the corresponding 2D structure [Fig. 9(a)], possessing better electronic characteristics. In particular, smaller A cations favor the formation of the 2D phase over the 0D one [Fig. 9(c)].¹⁰² For example, according to numerous reports, $\text{MA}_3\text{Sb}_2\text{I}_9$ (ionic radius ~ 180 pm) forms in the 0D phase whereas $(\text{NH}_4)_3\text{Sb}_2\text{I}_9$, $\text{Rb}_3\text{Sb}_2\text{I}_9$, and $\text{K}_3\text{Sb}_2\text{I}_9$ (ionic radius ~ 150 pm) in the 2D polymorph. It is worth noting that the 0D and 2D phases of Cs^+ (ionic radius 167 pm) have similar formation energies, and which polymorph is formed depends on the synthesis conditions.

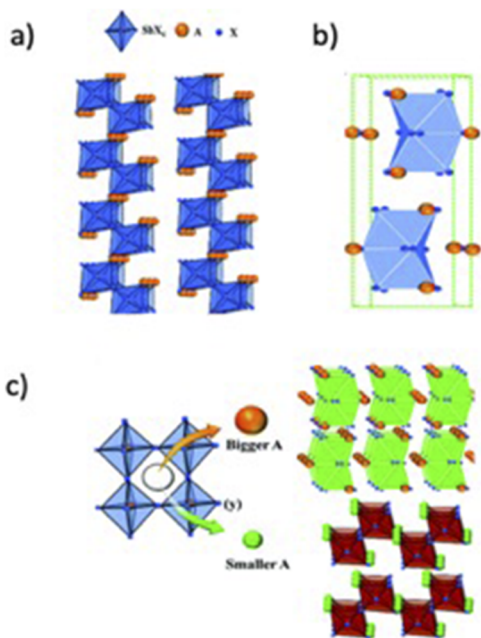


FIG. 9. (a) Layered (2D) structure of $A_3Sb_2X_9$. (b) (0D), face-sharing fused biocathedron dimer structure of $A_3Sb_2X_9$; (c) schematic representation showing the impact of the A cation having a different ionic radius: A bigger A cation (X) results in the 0D dimer structure and a smaller A (Y) one in the 2D layered structure phase. Adapted with permission from Nie *et al.*, *Energy Environ. Sci.* **13**(8), 2363–2385 (2020). Copyright 2020 Royal Society of Chemistry.

The 2D $A_3B_2X_9$ phases can be stabilized by alloying halides, I with Br or Cl, favoring a change in the structure from face- (0D phase) to corner-sharing $[BX_6]^{3-}$ octahedra (2D phase). For instance, the authors of the work of Mie *et al.* obtained 0D to a 2D structure transition via fractional substitution of iodide with chloride in $Cs_3Sb_2I_9$ (leading to $Cs_3Sb_2I_{9-x}Cl_x$) with a low-temperature, solution-based deposition process.¹⁰³

2D $Cs_3Sb_2I_9$ has attracted significant interest owing to its lowest bandgap, among its other halide derivatives ($Cs_3Sb_2Cl_9$, $Cs_3Sb_2Br_9$), which results in potentially higher performance of OPV due to higher absorption coefficient at 1.5 AM conditions ($>10^5 \text{ cm}^{-1}$). However, similar to LHPs, $Cs_3Sb_2X_{9-a}Y_a$ possesses a compositional tunable bandgap, which makes this material very interesting for IPV applications. DFT band structure calculations showed that the VBM of 2D $Cs_3Sb_2I_9$ is composed of mixed I p and Sb s orbitals, whereas CBM is mainly derived from Sb p states [Fig. 10(a)].¹⁰⁴ It is rather interesting to note that this band structure strongly mimics the 2D layered ($N = 4$) lead-halide counterpart (Cs_2PbI_4), where the VBM consists of hybridized filled Pb-6s and I-5p orbitals, while the CBM mainly consists of empty Pb-6p orbitals [Figs. 10(c) and 10(d)].^{105,106} Thus, one expects 2D $Cs_3Sb_2I_9$ to deliver similar structural characteristics and optoelectronic properties to its lead-based counterpart. The 2D $Cs_3Sb_2I_9$ does not only display a lower direct bandgap of $\sim 2 \text{ eV}$ but also shows improved band dispersion compared to its 0D counterpart, which, on the contrary, has a much larger indirect bandgap of 2.4 eV [Fig. 10(b)]. Furthermore, it has been verified by the space charge limited current (SCLC) that 2D $Cs_3Sb_2I_9$ thin

films have a hole mobility of $6.81 \text{ cm}^2/\text{V s}^{-1}$, which is almost double that in 0D polymorph, which is also indicative of the reduced carrier effective mass in the case of the 2D phase.

Despite the positive aspects highlighted above, theoretical studies of defect properties by Saparov and co-workers have suggested the presence of dominant deep-level defects in 2D $Cs_3Sb_2I_9$.¹⁰⁴ Out of the studied intrinsic point defects, like cation vacancies (V_{Cs} , V_{Sb}), iodide interstitial (I_i), Cs on Sb cation substitution (Cs_{Sb}), anion-on-cation antisites (I_{Cs} , I_{Sb}), iodide vacancy (V_I), cation interstitial (Cs_i , Sb_i), Sb on Cs substitution (Sb_{Cs}), and cation-on-anion antisite substitution (Cs_I , Sb_I), the thermodynamically dominant defects are V_{Cs} , I_i , I_{Sb} , Cs_i , and V_I ; among these, only Cs_i and V_{Cs} produce shallow levels, whereas I_i , I_{Sb} , and V_I produce deep levels according to the calculated charge transition levels.

These defects have also been considered responsible for the limited stability of both 0D and 2D polymorphs of $Cs_3Sb_2I_9$ to humidity, air, heat, and light.¹⁰⁷ The authors identified the loss of iodine from the system as the prime reason for the degradation of the $Cs_3Sb_2I_9$ system. Unfortunately, no theoretical explanation has yet been provided to help devise strategies to counteract this phenomenon. Finally, mild fabrication conditions favor the formation of 0D $Cs_3Sb_2I_9$, while to obtain the 2D polymorph, specialized techniques, such as thermal evaporation or treatments at temperatures $\geq 230^\circ\text{C}$, must be used.¹⁰⁸

Halide alloying is proposed to overcome some of the limitations of $Cs_3Sb_2I_9$ without impairing the intriguing characteristics of the material. According to theoretical investigations of Park and Hong, 33% Cl substitution in $Cs_3Sb_2I_9$ leads to formation of stable 2D $Cs_3Bi_2I_6Cl_3$ and was accompanied by 0.22 eV bandgap reduction compared to 0D $Cs_3Bi_2I_9$.¹⁰⁹ While reduction of the bandgap is neither important nor desirable for IPV, the authors of the work of Jiang *et al.* also reported that partial replacement of iodide with chloride in the $Cs_3Sb_2I_9$ lattice suppresses the formation of the 0D phase.¹¹⁰ The previous observations were supported by Peng and co-workers, who reported a PCE of 2.15% for high-quality 2D $Cs_3Sb_2Cl_xI_{9-x}$ films.¹⁰¹ However, none of the theoretical calculations report the composition–structure–optical property relations specifically for $Cs_3Sb_2I_{9-x}Cl_x$ PV cells. However, a recent theoretical study carried out by Pradhan *et al.* showed that a minimal (two atoms per formula structure) substitution of Br in $Cs_3Sb_2Cl_9$, $Cs_3Sb_2Cl_7Br_2$, led to an indirect (2.28 eV)-to-direct (2.17 eV) bandgap transition.¹¹¹ The splitting of p -states of halides and Sb just above the Fermi level induced by change in the terminal Cl/Br–Sb–Cl/Br bond angle is observed to be the primary reason for transition of the band from an indirect to direct type with Br substitution. Hence, halide alloying does appear to be an effective strategy to obtain high-quality 2D structures and, henceforth, materials that can deliver high PCE. Despite the progress, the still limited efficiency raises numerous questions about charge transport between the material and the HTL/ETL. Hence, extensive and systematic theoretical research is important for the progress of this field.

III. HEAVY Pnictogen-BASED PEROVSKITES AND PIMs: THE MODEL CASE OF THE $Cs_2AgBiBr_6$ DP

In the frame of the three PIMs discussed within this review, the ionic structure of the $Cs_2AgBiBr_6$ DP is undoubtedly the closest to the original ABX_3 perovskite structure. In this material, the

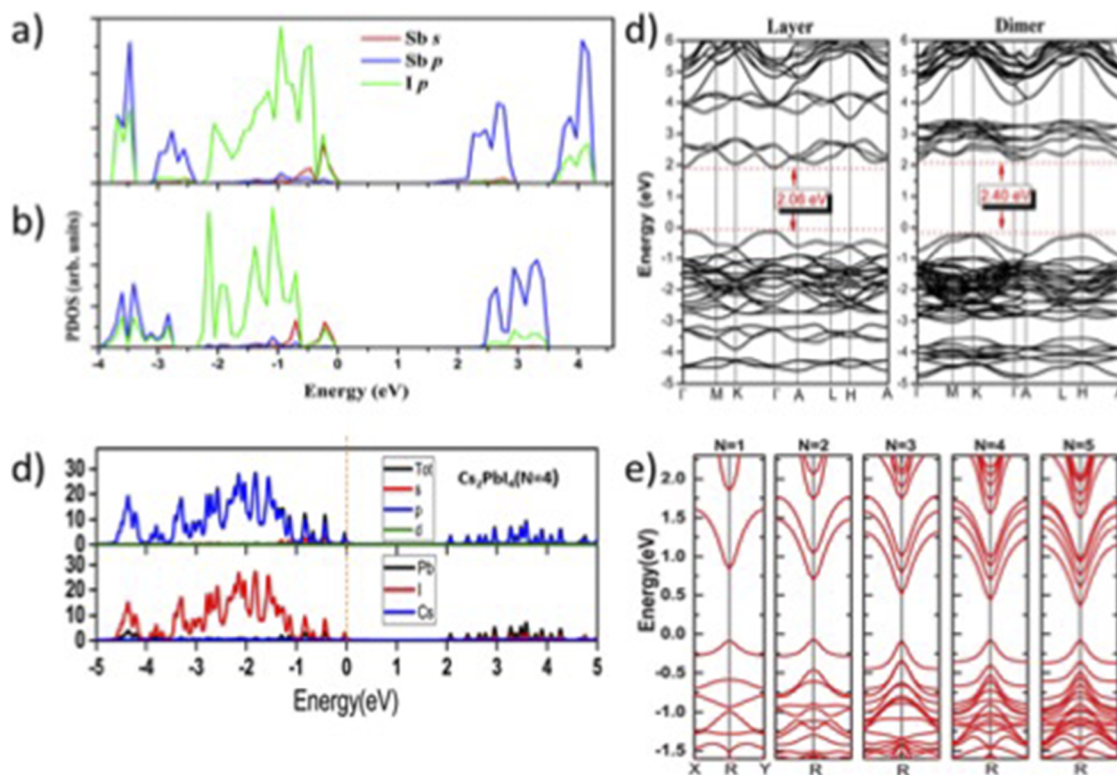


FIG. 10. Partial density of states (PDOSs) of (a) layered and (b) dimer modifications of $\text{Cs}_3\text{Sb}_2\text{I}_9$, respectively. (c) In the panel, the corresponding band structures are shown. Adapted with permission from Saporov *et al.*, Chem. Mater. **27**(16), 5622–5632 (2015). Copyright 2015 Author(s), licensed under a Creative Commons Attribution 4.0 License. (d) PDOSs of Cs_2PbI_4 ($N = 4$); (e) calculated band structures of Cs_2PbI_4 ($N = 1-4$). Reproduced with permission from L. Zhang and W. Liang, J. Phys. Chem. Lett. **8**(7), 1517–1523 (2017). Copyright 2017 American Chemical Society.

divalent Pb^{2+} cations on the B-site are substituted by a (theoretically) equal ratio of monovalent Ag^+ and trivalent Bi^{3+} cations, to form a perovskite-like structure in which $[\text{AgBr}_6]^{5-}$ and $[\text{BiBr}_6]^{3-}$ octahedra are arranged in an alternating fashion [see Fig. 2(a)]. Accordingly, this material and materials in which analogous substitutions are performed are named DPs or elpasolites. As $\text{Cs}_2\text{AgBiBr}_6$ is a fully inorganic DP and Ag^+ and Bi^{3+} are very inert cations, this material is generally characterized by high stability to environmental conditions. In contrast to its lead-containing counterparts, $\text{Cs}_2\text{AgBiBr}_6$ possesses an indirect bandgap that is reported to be between 2 and 2.2 eV.^{66,112,113} Although this bandgap energy is only slightly exceeding the optimum value for IPVs (see Fig. 1), its indirect character and other optoelectronic properties of this material, like the strong electron–phonon coupling (described in detail in Sec. II),^{114,115} and the fast surface carrier recombination,¹¹⁶ prevent it from achieving large PCEs as a light-harvesting material in PPVs. Still, since $\text{Cs}_2\text{AgBiBr}_6$ is one of the earliest PIMs investigated,³⁶ extensive research on this material can serve as the basis to synthesize and characterize related PIMs, which can help overcome the efficiency-hampering features of $\text{Cs}_2\text{AgBiBr}_6$. For this reason, we summarize here relevant information about the state-of-the-art research progress on $\text{Cs}_2\text{AgBiBr}_6$, to show from which of these findings other PIMs can benefit. It is important to note that, in the

vast majority of reports that studied $\text{Cs}_2\text{AgBiBr}_6$ as light-harvesting material, the PV devices were not characterized under indoor but rather under outdoor irradiation. Still, $\text{Cs}_2\text{AgBiBr}_6$ IPVs will benefit from investigations about the material's crystallization behavior, its optoelectronic properties, or the dependence of its bandgap on the structure. Moreover, research on entire solar cells will support the investigation on IPVs, owing to $\text{Cs}_2\text{AgBiBr}_6$'s suitable bandgap for the scope. For example, recently, some of us reported on a “green” $\text{Cs}_2\text{AgBiBr}_6$ -based solar cell architecture by substituting the gold back electrode and HTL with a single layer of carbon black that was obtained from upcycled 5-year-old used car tires and deposited by ultrasonic spray-coating from atoxic isopropanol with no additives (Fig. 11).¹¹⁷ This approach of utilizing an end-of-waste material, in conjunction with a sustainable PIM as a light-absorber, drastically reduces production costs and toxicity concerns for devices expected to operate within households and at the same time enables the fabrication of solar cells with exceptionally high open-circuit voltages (V_{OC}).

$\text{Cs}_2\text{AgBiBr}_6$ is prepared analogously to its lead counterparts from solution, e.g., via spin-coating,^{118,119} by evaporation, even single-source evaporation,¹²⁰ or by pulsed laser deposition (PLD).¹²¹ The first critical step to creating well-performing PVs is to fabricate homogeneous, pinhole-free perovskite thin films

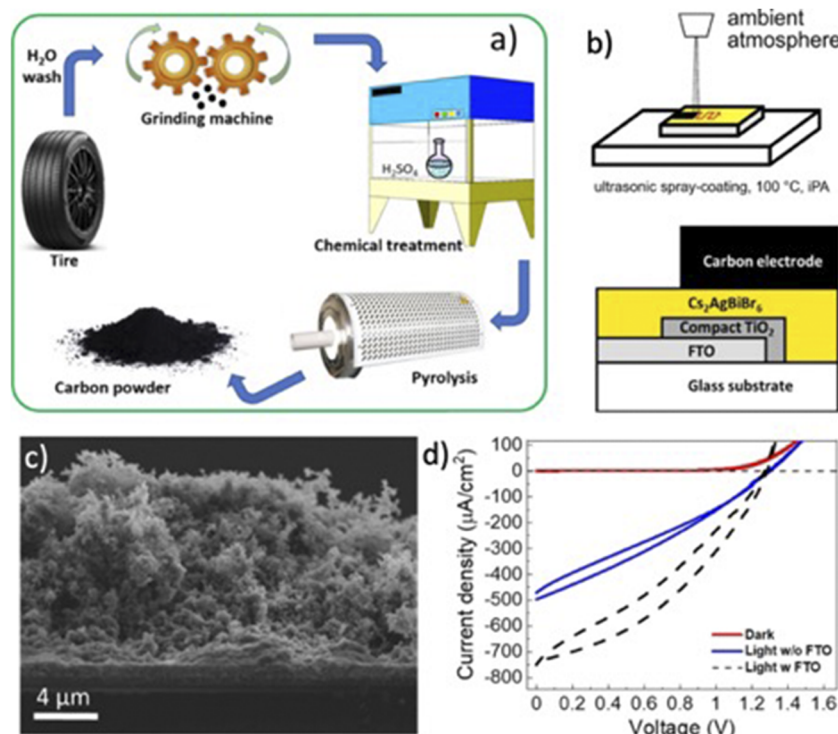


FIG. 11. (a) Process for the production of an end-of-waste carbon black powder from waste tires. (b) Schematic of the ultrasonic spray-coating method used to deposit the carbon electrode on Cs₂AgBiBr₆ solar cells. (c) Cross-section scanning electron microscope image of the resulting solar cell. (d) Current density-voltage characteristics of the device in dark, light, and after application of gentle pressure on top of the carbon electrode with a conductive glass slide. Adapted with permission from Schmitz *et al.*, ChemSusChem **15**(22), e202201590 (2022). Copyright 2022 Author(s), licensed under a Creative Commons Attribution 4.0 License.

that feature large grain sizes, thus reducing the number of grain boundaries, which serve as dominant nonradiative recombination sites and as main channels for ion transport.¹²² To reduce this degradation-inducing ion diffusion during long-term operation,¹²³ the authors of the work of Li *et al.* added the ionic liquids 1-butyl-1-methylpyrrolidinium chloride (BMPyCl) and 1-butyl-3-methylpyridinium chloride (BMPyCl) to interact with the Br⁻ ions, pinning them in the perovskite structure.¹²⁴ This drastically improved the resulting device long-term stability.

Moreover, control over the PIMs crystallization process is crucial to fabricate high-quality thin films. The grain growth and homogeneity of PIM thin films can either be positively affected by introducing additives, such as thiourea (TU),¹¹⁸ formamidine acetate,¹¹⁹ an (HBr)-assisted synthesis,¹²⁵ or by covering the ETL with methylammonium chloride before spin-coating Cs₂AgBiBr₆.¹²⁶ The latter does not only enhance the crystallization but also reduces trap-assisted recombination by facilitating the electron extraction from the perovskite to the ETL.¹²⁶ A more fundamental method to enhance the film quality is to perform solvent engineering. The authors of the work of Abdelsamie *et al.* were able to obtain detailed insights into the crystallization process when antisolvent dropping was performed during the spin-coating process, using *in situ* spectroscopy and *in situ* grazing incidence wide-angle x-ray scattering (GIWAXS).¹²⁵ They found that antisolvent

dropping increased the film homogeneity by inducing instantaneous supersaturation and crystallization of the wet film. Furthermore, not only does antisolvent dropping require a hot casting but also the dropping time within a narrow window is critical to creating pinhole-free films.

Since the bandgap of Cs₂AgBiBr₆ is too large even to achieve an optimum PCE in IPV, various options to decrease it have been investigated. Analogous to lead-based perovskites, ionic substitution, especially anion exchange, is a promising attempt to tune the bandgap. In this regard, substituting Br⁻ by I⁻ would reduce the material's bandgap. Simulations by the authors of the work of Alla *et al.* indicate that Cs₂AgBiI₆ could reach up to ~29% PCE in combination with suited ETL and HTL in OPVs. Despite this, pure Cs₂AgBiI₆ has not found use in real devices due to its unstable nature.¹²⁷ On the contrary, a partial substitution of Br⁻ by I⁻ via anion exchange utilizing methylammonium iodide (MAI) during post-treatment to fabricate CsAgBiBr_{6-x}I_x (0 ≤ x ≤ 4) thin films led to a bandgap reduction by up to 0.3 eV for an iodide content of x = 4 [Fig. 12(a)].¹²⁸ Shifting the bandgap toward larger values is also possible by substituting Br⁻ with Cl⁻ instead of I⁻. The authors of the work of Ahn *et al.* showed this for their mechanochemically synthesized CsAgBiBr_{6-x}Cl_x (0 ≤ x ≤ 6) powders, gradually blue-shifting the material's absorption as well as emission spectra with increasing Cl⁻ content.¹²⁹ Interestingly, Raman spectral analyses pointed out

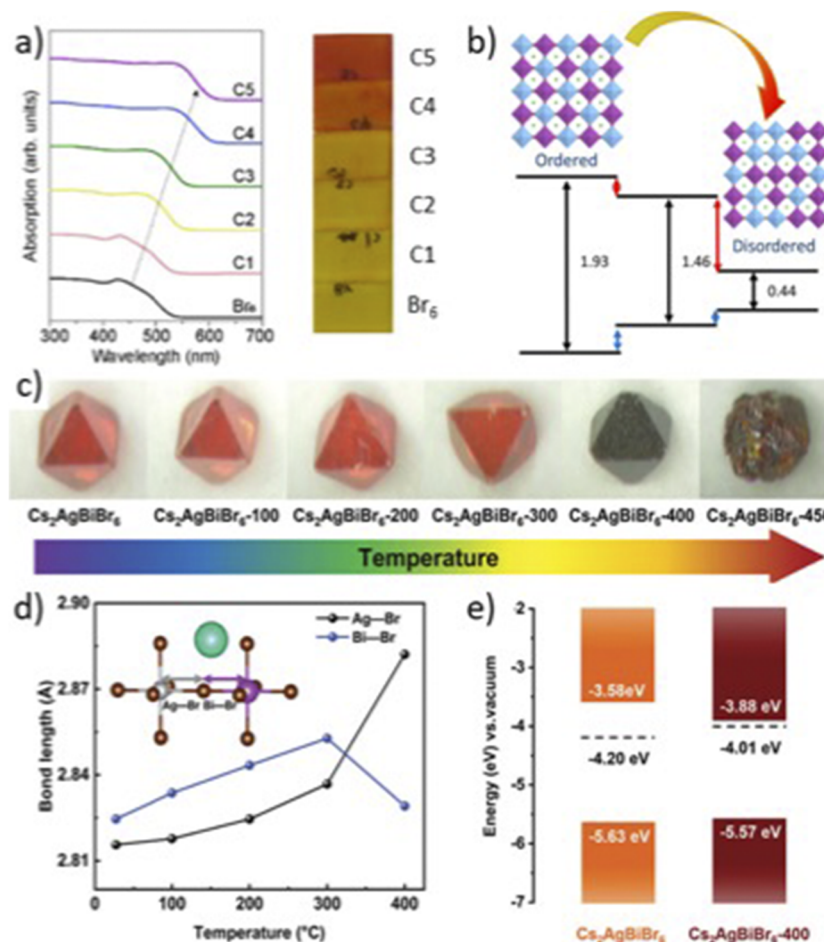


FIG. 12. (a) Bandgap tuning through halide exchange via MAI post-treatment. Adapted with permission from Wu *et al.*, ChemSusChem **14**(20), 4507–4515 (2021). Copyright 2021 Wiley. (b) Schematic bandgap dependency on the degree of disorder in the [BiBr₆]³⁻ and [AgBr₆]⁵⁻ octahedra for Cs₂AgBiBr₆. Reproduced with permission from Yang, Zhang, and Wei, J. Phys. Chem. Lett. **9**, 31–35 (2018). Copyright 2018 American Chemical Society. (c) Color of single crystals as well as (d) Ag–Br and Bi–Br bond lengths for varying annealing temperatures, and (e) effect of 400 °C annealing temperature on VB, CB, and Fermi energy. Reproduced with permission from Zhang *et al.*, Small **18**(24), 2201943 (2022). Copyright 2022 Wiley.

that the formation of Br⁻-rich and Cl⁻-rich octahedra is preferred rather than a homogeneous alloy.¹³⁰ Not only the anionic but also the cationic substitution of Bi³⁺ can have an impact on the bandgap. The incorporation of Sb³⁺ on the Bi³⁺ site can lead to a reduction of the bandgap.¹³¹ However, Sb³⁺ hardly substitutes Bi³⁺ except when utilizing a mechanochemical or a spray-drying synthesis that allows up to 40% of Sb³⁺ substitution.¹³¹

As mentioned in Sec. II, composition alternation is not a necessity to tune the material's bandgap. Due to the special property of Cs₂AgBiBr₆, containing a mixture of two different B-site octahedra, a variation of their structural arrangement, too, strongly influences its bandgap. First-principles calculations show that the large indirect bandgap that is typically observed for Cs₂AgBiBr₆ exists due to the highly ordered structure of alternating [BiBr₆]³⁻ and [AgBr₆]⁵⁻ octahedra.^{68,132} However, as soon as antisite-type defects are created, changing the ordered structure to a disordered one, not only does

the bandgap decrease gradually with the degree of disorder, reaching a minimum of 0.44 eV for a fully disordered structure,⁶⁸ as it is depicted in Fig. 12(b), but also the bandgap character changes from indirect to direct¹³² or pseudodirect.⁶⁸ Since the energy difference per mixed cation site between the ordered and disordered Cs₂AgBiBr₆ is quite large with a value of 0.141 eV, most reported thin films and single crystals possess the ordered structure and therefore the unwanted large indirect bandgap.

The authors of the work of Zhang *et al.* proved this theoretical model experimentally by annealing a Cs₂AgBiBr₆ single crystal at various temperatures. They observed a shift in UV–vis absorption spectra and photoluminescence spectra as well as a coherent change of the single crystal color from red to black at 400 °C, depicted in Fig. 12(c), that corresponded with a bandgap reduction from 2.05 to 1.69 eV.¹³³ Lower temperatures from room temperature up to 300 °C did not induce any change in optical properties and an

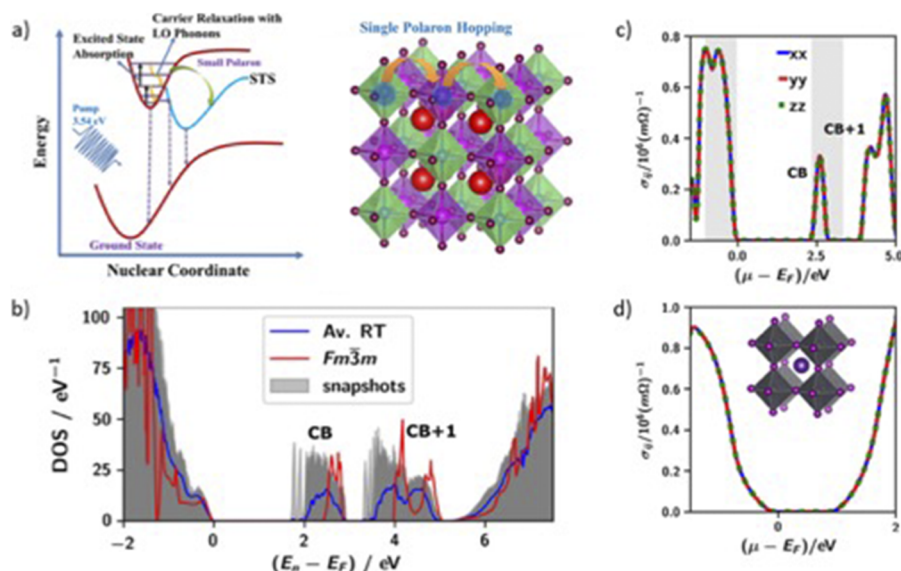


FIG. 13. (a) Polaron hopping mechanism in $\text{Cs}_2\text{AgBiBr}_6$: Excited carriers relax via coupling with longitudinal optical (LO) phonons. Distortion of the soft $\text{Cs}_2\text{AgBiBr}_6$ lattice triggers acoustic phonons in which the carriers are self-trapped. This ultrafast trapping process favors the polaron hopping transport. Reproduced with permission from Tailor *et al.*, J. Phys. Chem. Lett. **14**(3), 730–736 (2023). Copyright 2023 American Chemical Society. (b) Comparison of $\text{Cs}_2\text{AgBiBr}_6$ DOS at $T = 0 \text{ K}$ and room temperature, (c) electrical conductivity tensors calculated for $T = 300 \text{ K}$ for $\text{Cs}_2\text{AgBiBr}_6$ and for (d) CsPbI_3 . Reproduced with permission from J. Gebhardt and C. Elsässer, Phys. Status Solidi B **259**(8), 2200124 (2022). Copyright 2022 Wiley.

annealing temperature of 450°C led to the decomposition of the material, which follows the thermal stability limit of 410°C , reported by Dakshinamurthy and Sudakar.¹³⁴ For the 400°C annealed single crystal, a large change of Ag–Br and Bi–Br bond lengths occurred, shown in Fig. 12(d), that could not be attributed to temperature-induced lattice expansion but was explained by the formation of Ag_{Bi} and Bi_{Ag} antisite defects.¹³³ As a result, those antisite defects broaden the band edges, change the energy levels of VBM and CBM, which could be observed by x-ray photon spectroscopy measurements, and therefore decrease the bandgap [Fig. 12(e)].

Finally, a hydrogenation of $\text{Cs}_2\text{AgBiBr}_6$ thin films, resulting from interstitial doping with atomic hydrogen atoms, also strongly affects their bandgap.^{60,61} Using this method, the group of Sui was able to reduce the bandgap from 2.18 to 1.64 eV, to create $\text{Cs}_2\text{AgBiBr}_6$ OPVs with a record PCE of 6.37%.⁶⁰ They also observed that the hydrogenation treatment improved the material's charge carrier concentration, mobility, and lifetime. Numerical simulations show that an optimization of the ETL toward a $\text{SnO}/\text{ZnO}_{0.4}\text{S}_{0.6}$ double ETL system as well as an increased $\text{Cs}_2\text{AgBiBr}_6$ film thickness could increase the OPV PCE to 14.23% and a PCE of 15.61% at a lower intensity of $40 \text{ mW}/\text{cm}^2$, which hints at the perspective use of this architecture in IPVs.

Besides the optimum band alignment between $\text{Cs}_2\text{AgBiBr}_6$ and ETL as well as HTL, respectively, and the width of the bandgap, its character, followed by other intrinsic optoelectronic properties have deeply been investigated to reveal the reason for its weak PV performance of $\text{Cs}_2\text{AgBiBr}_6$. Recent electrochemical analyses such as temperature-dependent electrochemical spectroscopy,¹³⁶ temperature-dependent ac conductivity analysis,¹¹⁵ and field-effect transistor measurements¹²² revealed that the dominant conduction

mechanism in this material is thermally activated polaron hopping, which is depicted in Fig. 13(a). Additionally, Gebhardt and Elsässer used a self-energy-corrected DFT method to investigate the electronic structure of $\text{Cs}_2\text{AgBiBr}_6$ in which they emphasized that the inclusion of structural dynamics broadened the CB and therefore decreased the indirect bandgap, an aspect, which many calculations neglect but is crucial for an accurate description of its electronic structure, as shown in Fig. 13(b).¹³⁵ Furthermore, they debated the low DOS in CB, as well as the absence of states between the CB and the next band CB + 1, is the cause of the low conductivity of $\text{Cs}_2\text{AgBiBr}_6$, since charge extraction in photovoltaics does not only rely on charge carriers that occupy the band edges. While the conductivity in the VB of $\text{Cs}_2\text{AgBiBr}_6$ [Fig. 13(c)] is like that of CsPbI_3 [Fig. 13(d)], its CB conductivity is significantly lower, which results in PCEs for $\text{Cs}_2\text{AgBiBr}_6$ that are an order of magnitude lower than those of LHP solar cells.

In summary, these investigations show that there are unexploited aspects of $\text{Cs}_2\text{AgBiBr}_6$ for PVs, which is contrasted by its unfavorable intrinsic optoelectronic properties. Still, the detailed analyses of this material can pave the way for related PIMs that, by clever design, can overcome the limits of $\text{Cs}_2\text{AgBiBr}_6$.

IV. EMERGING PIMs: THE CASE OF THE BIOI OXYHALIDE

The BiOI oxyhalide PIM is at the forefront of many different research efforts, trying to implement it both in (I)PV⁶ and also in photoelectrochemical systems for the solar-driven splitting of water to produce hydrogen or for the reduction of CO_2 .¹³⁷ Bi- and Sb-based chalcogenides are also investigated for similar

purposes. Although we do not discuss them here, we want to address the reader with another interesting and very recent review on the topic.¹³⁸

The BiOI semiconductor has a layered structure [see Fig. 2(b)], with layers being held together by weak van der Waals forces along the *c*-axis, analogous to its sister halide species like BiI₃ and Ag₃BiI₆. Although the 2D structure is not generally considered favorable for light-induced charge separation processes, this issue could become almost irrelevant when a semiconductor growth strategy has been properly developed to induce the orientation of the *c*-axis parallel to the substrate (and thus to the ETL and HTL). The authors of the work of Crovetto *et al.* have reported a detailed analysis of the three sister bismuth halide semiconductors (i.e., BiOI, BiI₃, and Ag₃BiI₆) in terms of electronic properties, thin film growth, and PV performance in single-junction solar cells.¹³⁹ All three of them have common features, such as the low to moderate temperature suitable for their synthesis [here carried out through oxy(iodization) of metallic precursors], the optimal bandgaps for top absorbers in tandem solar cells, and a relatively deep VB. However, this survey shows that texture control, i.e., crystals' orientation, could only be achieved partially for BiOI and BiI₃, with the former showing overall the best PV parameters, with a maximum PCE of 0.66%.

The first consistent contribution to making the PV performance obtained from BiOI-based solar cells competitive with other emerging semiconductors has been given in the work of Hoyer *et al.*

in 2017.⁹⁷ In this milestone work, the authors have investigated all-inorganic devices with configuration ITO|NiO_x|BiOI|ZnO|Al [Fig. 14(b)], in which the BiOI photoabsorber layer was grown by chemical vapor transport (CVT), a process with excellent perspectives for industrialization. The thus produced BiOI layers resulted to be very stable under standard environmental conditions (20–25 °C ambient temperature, 46%–67% relative humidity, and standard laboratory illumination) without any encapsulation, as shown by the x-ray diffraction (XRD) patterns measured over 197 days [Fig. 14(a)]. The stability was confirmed by a direct comparison within entire PV architectures with a classical LHP, i.e., MAPL. While the latter is well known for its strong sensitivity to moisture, causing a progressive PCE decay within a few minutes of operation, the BiOI-based devices were found to maintain their initial performance for up to 3 days [Fig. 14(c)]. Although the best PCE values were lower than 2%, an impressive external quantum efficiency (EQE) of 80% was measured, thanks to the densely packed morphology of the NiO_x HTL and BiOI layers. In addition, the first evidence of the better suitability of this semiconductor for PV operation under low-intensity illumination comes from the observed trend in Fill Factor (FF) reported in Fig. 14(c): This figure of merit is indeed at its maximum at the lowest tested light intensity. The observation agrees with the trends in shunt and series resistances, indicating an increase in photogenerated carrier recombination when carrier densities rise, at elevated light intensity.

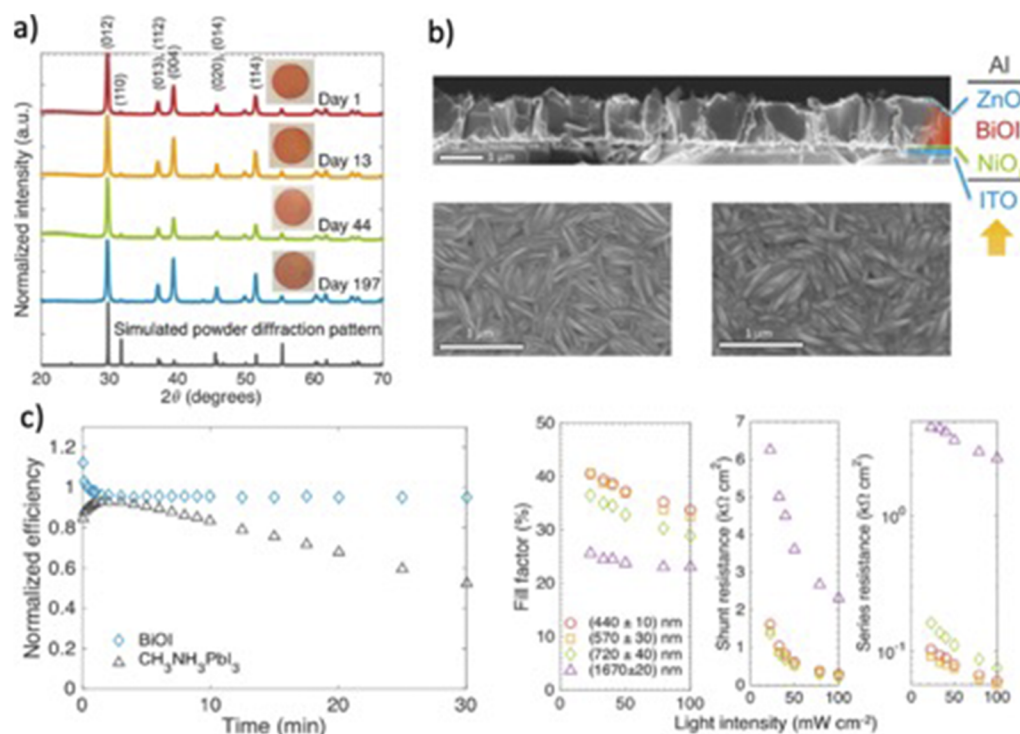


FIG. 14. Characterization of CVT BiOI thin films and solar devices. (a) Long-term stability of the CVT BiOI films as determined by x-ray diffraction on films kept in air for a prolonged time. (b) Solar cell architecture as seen by cross-section SEM image and BiOI film morphology as seen in top-view SEM images (left: sole BiOI; right: ZnO further grown onto BiOI). (c) Performance of BiOI and CH₃NH₃PbI₃ devices over time under constant 1 sun illumination (left) and effect of light intensity onto cell parameters (right). Adapted with permission from Hoyer *et al.*, Adv. Mater. **29**(36), 1702176 (2017). Copyright 2017 Author(s), licensed under a Creative Commons Attribution 4.0 License.

The same group achieved a preferential orientation along the c -axis with higher control over the BiOI layer. This allowed a shift of the V_{OC} from 0.7 to 0.9 V, which is near the calculated theoretical limit of 1.34 V.¹⁴⁰ Tuning of the orientation was possible thanks to the variation of operative conditions used for CVT: In a nucleation-dominated regime, the c -axis orientation results are favored [Fig. 15(b)] compared to a grain-growth dominated one, in which a/b -axis orientation is preferred [Fig. 15(a)]. This morphological change has a direct influence on solar cell performance, as shown in Figs. 15(c) and 15(d) with higher V_{OC} measured in devices featuring the absorber in preferential c -axis orientation. However, this arrangement is detrimental to charge extraction, as clearly shown by the concomitant decrease in current density [Fig. 15(c) and 15(e)], as the ETL and HTL are not directly connected with the higher mobility crystal planes. The authors concluded that for the specific case of (I)PV applications, a combination of a/b -axis and c -axis oriented platelets might be necessary within the photoactive layer. Alternatively, a back-contact architecture may be explored using c -axis oriented BiOI. From this last orientation, other applications might benefit, for example, field-effect transistors.¹⁴¹

Recently, there has been a growing interest in demonstrating the use of solution-processing methods to fabricate films of BiOI suitable for PV. Soga and co-workers have pioneered the successive ionic layer adsorption and reaction (SILAR) method carried out on a spin-coating platform (previously SILAR was reported only through dip-coating) as a simple and “green” technique to prepare BiOI thin films suitable for PV.¹⁴¹ In this first contribution, 300 nm thick films of BiOI on FTO were obtained by applying 30 reactive cycles of SILAR employing water solutions of $\text{Bi}(\text{NO}_3)_3 \cdot 5\text{H}_2\text{O}$ and KI as the alternatively-deposited precursors, although no indications of annealing treatment are provided. The films were used in

dye-sensitized solar cell-like configurations as photoanodes with a liquid iodide/triiodide electrolyte couple, delivering very low PCE (0.05%). Improvements in device performance were obtained by applying a 100 °C 1 h annealing treatment in air on the spin-SILAR deposited films, reaching a PCE of slightly more than 0.1%.¹⁴²

The most remarkable and recent result obtained from solution-processing of BiOI is undoubtedly the one presented in work of Feeney *et al.*, in which solar cells with the same all-inorganic architecture as the one employed in the work of Hoyer *et al.* were fabricated uniquely resorting to solution-based deposition of both the BiOI photoactive layer and the NiO_x HTL and ZnO ETL.¹⁴³ Here, the authors have resorted to the templated conversion of bismuth iodide thin films through hydrolysis in a methanol/water bath, in a low-temperature (<100 °C), carbon-free iterative process, which is depicted in Fig. 16(a). In detail, they first spin-coated BiI_3 solution onto substrates that were annealed, afterward. Then, they submerged the films in a 1:1 mixture of methanol and water to convert the BiI_3 to BiOI and then rinsed it two times in pure methanol, before drying the thin films at 100 °C [Fig. 16(a)]. The nickel oxide HTL was instead prepared via sol-gel, while the ZnO ETL was obtained from direct spin-coating deposition of ZnO nanoparticles. In similar solar cells, the PCE was strongly influenced by the number of BiOI layers (and partially by that of the ETL), with a peak performance at three layers of around 0.7% [Fig. 16(a)]. In the attempt to exploit the effect of a preferential a/b -axis orientation in the BiOI film, the authors further examined the effect of using sodium iodate as a templating agent and dopant in the hydrolysis bath. Figure 16(b) shows the effect of this treatment, with a relevant improvement happening only at 0.5 mM concentration of the iodate template, allowing partial vertical deposition of the BiOI grains within the films, which favors charge extraction. In this configuration, PCE

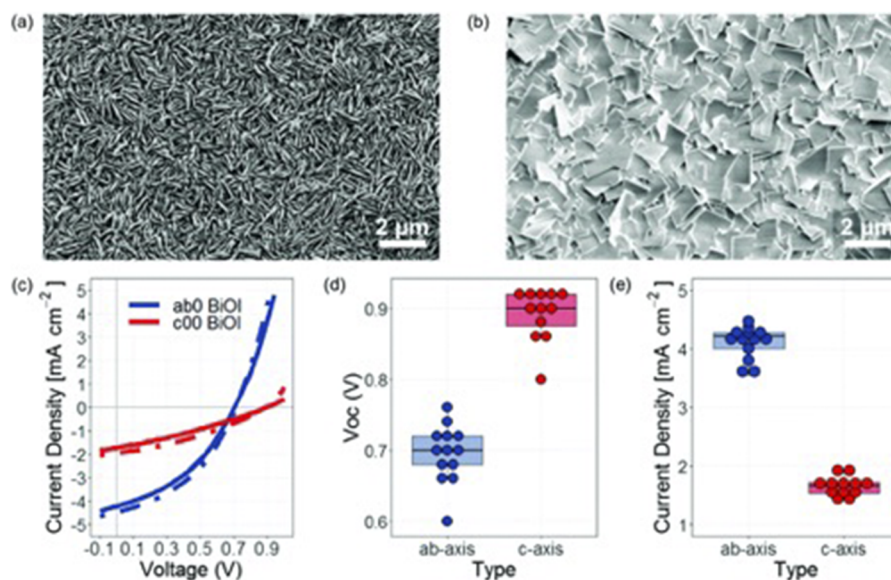


FIG. 15. Effect of controlled orientation of BiOI films on PV parameters. Morphology of thin film photo-absorbers having preferential (a) a/b -axis and (b) c -axis orientation. (c)–(e) PV data for the differently oriented films. Reproduced with permission from Jagt *et al.*, J. Mater. Chem. C 8(31), 10791–10797 (2020). Copyright 2020 Author(s), licensed under a Creative Commons Attribution 3.0 Unported License.

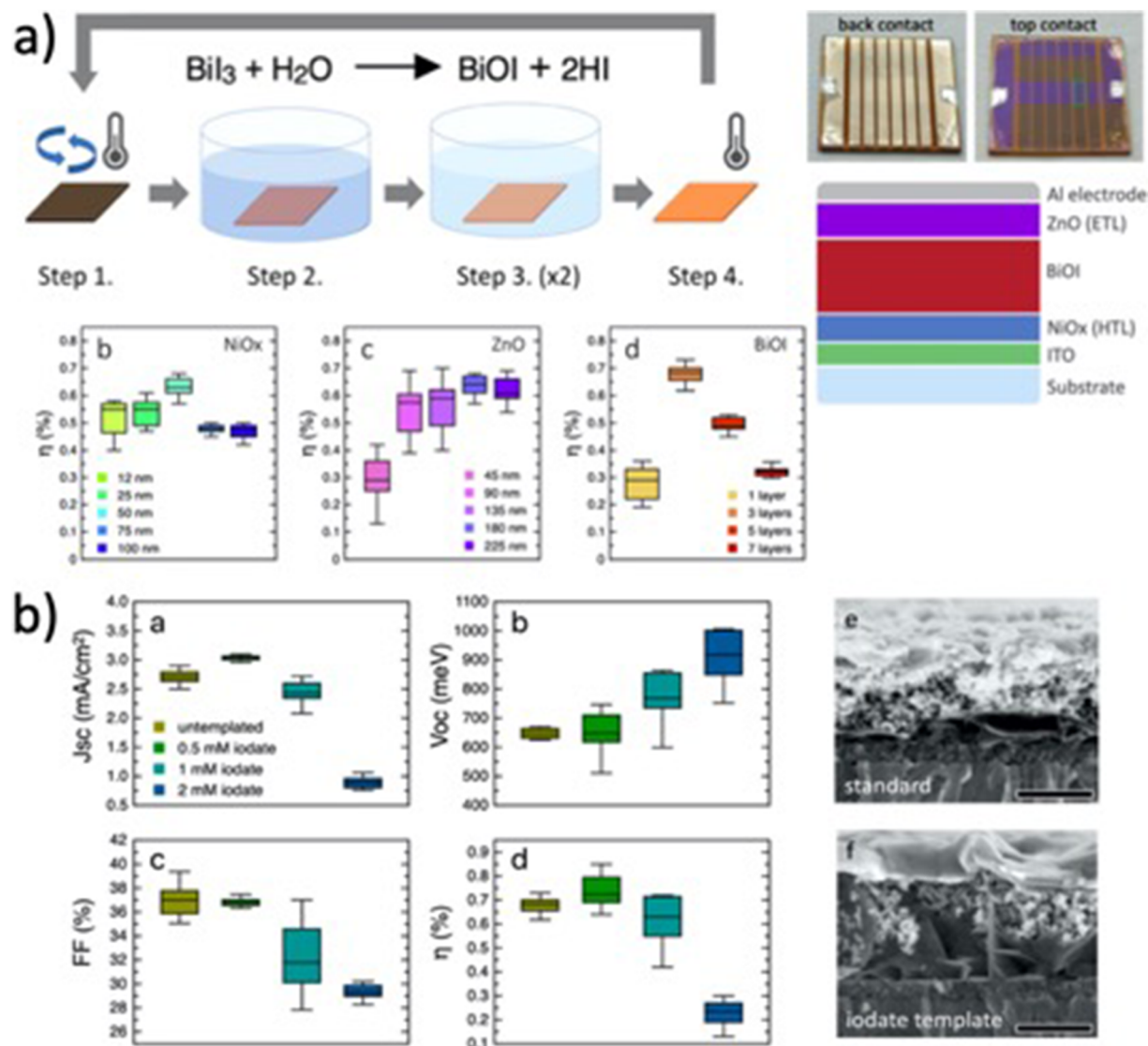


FIG. 16. Solution-processed BiOI thin films and devices. (a) Sketch of the deposition solution-based method, device architecture, and device characteristics at different thicknesses of the HTL, ETL, and photo-absorber. (b) Effect of iodate treatment on the device performance and crystalline grain orientation. Adapted with permission from Feeney *et al.*, *Nanotechnology* **34**, 305404 (2023). Copyright 2023 Author(s), licensed under a Creative Commons Attribution 4.0 License.

shifted to an average of 0.75%, thanks to the improvement in current density.

Ultimately, studies on bandgap tuning in BiOI might also allow to improve (I)PV performance of this material: Although the bandgap is optimal for indoor conditions, some slight changes might still allow it to reach better match with the spectrum of LEDs, for example. Moreover, narrowing the gap might pave the way for utilization of this material in outdoor applications. For the moment, very few reports have studied this issue and mostly about the use of the material as a photo(electro)catalyst: Zhang and Zhang have reported iodine self-doping of BiOI,¹⁴⁴ while the authors of the work of Ren *et al.* have studied the effect of defects engineering by acting on oxygen vacancies.¹⁴⁵ These are undoubtedly valuable

approaches, but likely they require a better rationalization for use in solar cells.

V. EMERGING PIMs: THE CASE OF $\text{Cs}_3\text{Sb}_2\text{I}_{9-x}\text{Cl}_x$

Considering antimony, when Sb replaces the Pb^{2+} cation in a metal-halide structure, being its stable cation trivalent, the resultant basic unit is of the form SbX_6^{3-} . The tridimensional shape is an octahedron, where the halides are coordinated by the A^+ cation, providing a PIM with a particular dimensionality and structure. $\text{A}_3\text{B}_2\text{X}_9$ usually crystallizes into zero-dimensional (0D) or two-dimensional (2D) species [for comparison, the $\text{A}_2\text{B}^{\text{III}}\text{X}_6$ DP is a tridimensional—3D—species, see Fig. 2(a)].

In particular, the fully inorganic $\text{Cs}_3\text{Sb}_2\text{I}_9$ PIM shows either a 0D dimeric form or a layer-shaped 2D one. Colloidal nanocrystals of this compound possess deeper defect levels compared to the lead-based counterparts, thus affecting electronic properties and requiring tight control over the defect's chemistry.¹⁴⁶ The 2D form has an optical bandgap of 2.05 eV and it is known for being notably stable in ambient conditions compared to MAPbI_3 . Colloidal $\text{Cs}_3\text{Sb}_2\text{I}_9$ nanocrystals are synthesized in a 2D structure with a high absorption coefficient, making them a valuable candidate for perovskite light absorbers. The substitution of the A^+ cation with other alkali metals like K or Rb creates other interesting light absorbers that were previously reviewed.¹⁴⁷

The solution-processed PIM forms the 0D structure, whereas the 2D form is obtained only when a solid or gas reaction takes place. The authors of the work of Saparov *et al.*¹⁰⁴ determined a bandgap of 2.05 eV, an absorption coefficient of 105 cm^{-1} , and an ionization potential of 5.6 eV. However, the high number of defects that form in both cases hugely affects the PV performances, thus providing a general PCE not higher than 1% in OPV architectures.¹⁰⁸ Furthermore, the high binding energy and the presence of an indirect bandgap of 2.5 eV cause low photocurrents.¹⁴⁸ In addition, it is worth mentioning that some recent studies have shown the possibility of tuning the optical bandgap exploiting high pressure: Narrowing of bandgap takes place from the initial 2.05 eV value to 1.36 eV, with proved recrystallization of the lattice.^{149,150} These studies demonstrate that a similar strategy can be useful for successful bandgap tuning of 2D structures.

For this reason, halide doping strategies have been applied, to improve optoelectronic properties of the $\text{A}_3\text{Sb}_2\text{I}_9$ PIM. One of these strategies resorts to the use of an HCl treatment. Cl^- anions are suspected to suppress the formation of Sb-I-Sb clusters, thus improving the crystallization process. In an important work, Zhou and co-workers demonstrated that, by incorporating a discrete amount of chloride into the methylammonium (MA) antimony iodide PIM ($\text{MA}_3\text{Sb}_2\text{I}_9$), a stabilized high-quality 2D layered phase film forms: By proper calculations, it is possible to demonstrate that chloride inclusion energetically favors the 2D layered phase with respect to the 0D dimeric phase, thus corroborating the experimental evidence (Fig. 17). This modification provides a PCE of more than 2% (2.15%–2.17% stabilized efficiency), that was the record for the time.¹¹⁰ In the same period, the authors of the work of Umar *et al.*¹⁵¹ proposed an antisolvent engineering methodology for stabilizing the planar phase, by adding a chloride additive like HCl, achieving a best PCE of 1.2%, probably lower due to the fast crystallization that produced smaller grains (not bigger than 50 nm).

For increasing the size of crystalline domains, chemical additives were employed, such as N-Methyl-2-pyrrolidone (NMP), thiourea (TU), and bis(trifluoromethane)sulfonimide lithium (the well-known LiTFSI used for 2,2',7,7'-Tetrakis[N,N-di(4-methoxyphenyl)amino]-9,9'-spirobifluorene (SPIRO-OMeTAD) HTLs p-doping). These compounds have the ability to form complexes with the trivalent antimony cation, thus retarding the perovskite formation process through the so-called "intramolecular exchange." The authors of the work of Yang *et al.*¹⁵² applied lithium bis(trifluoromethane)sulfonimide (LiTFSI) to $\text{MA}_3\text{Sb}_2\text{I}_{9-x}\text{Cl}_x$ films, reaching 3.34% PCE value and retaining 90% of the initial PCE after storing the solar cells under ambient conditions for 1400 h (Fig. 18). This result is very relevant, since the MA-based Sb(III)

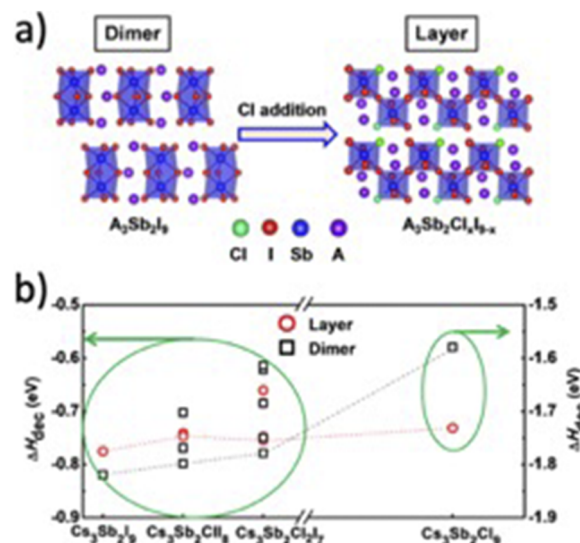


FIG. 17. Effect of chloride addition to dimeric/layered structural transition in Sb(III)-based PIMs. Reproduced with permission from Jiang *et al.*, J. Am. Chem. Soc. **140**(3), 1019–1027 (2018). Copyright 2018 American Chemical Society.

PIM usually suffers from chemical instability due to the presence of humidity, with respect to the all-inorganic sister species previously discussed.

TU and NMP are used for their capability of acting as Lewis bases as it is commonly reported for LHPs.¹⁵³ The presence of an intermediate complex [formed from the reaction with the Lewis acid, i.e., the Sb(III) halides] decreases the formation rate constant and thus also the rate of crystallization. However, the use of Lewis adduct phases is usually applied to organic–inorganic perovskites like MA or FA Pb perovskite.^{154–156} The authors of the work of Singh *et al.*¹⁵⁷ for the first time used the methodology with the full inorganic Sb-based PIM, by selectively adding either TU or NMP, achieving notable efficiencies (more than 1.5%), substantially given by increase in the photocurrent ($3.5\text{ vs }2.5\text{ mA cm}^{-2}$ for the control sample). The authors indicate that this improved efficiency originated from diminished charge carrier recombination, as confirmed by PL measurements and EQE analysis. However, the NMP additive is more effective than TU because the latter makes the films more vulnerable to environmental stress.

However, TU addition is beneficial for obtaining a tuned morphology. The orientation of crystals on the substrate surface indeed strongly affects the efficiency¹⁵⁸ of solar cells when 2D layers are considered. For this reason, several efforts were made in forcing vertical growth: In a very recent report,¹⁵⁹ 2D $\text{Cs}_3\text{Sb}_2\text{I}_{9-x}\text{Cl}_x$ film with (201) preferential orientation was realized. In this work, the authors added TU to the precursor solution and, thanks to the C=S group in this molecule, the crystallization dynamics were regulated so that the (201) orientation could be achieved instead of the unwanted (001) orientation, providing a stabilized efficiency of about 2.2%. In another relevant work,¹⁶⁰ 3,9-bis(2-methylene-(3-(1,1-dicyanomethylene)indanone))-5,5,11,11-tetrakis(4-hexylphenyl)dithieno[2,3-d:2',3'-d']-s-indaceno[1,2-b:5,6-b']dithiophene, usually abbreviated as ITIC additive, was used both as

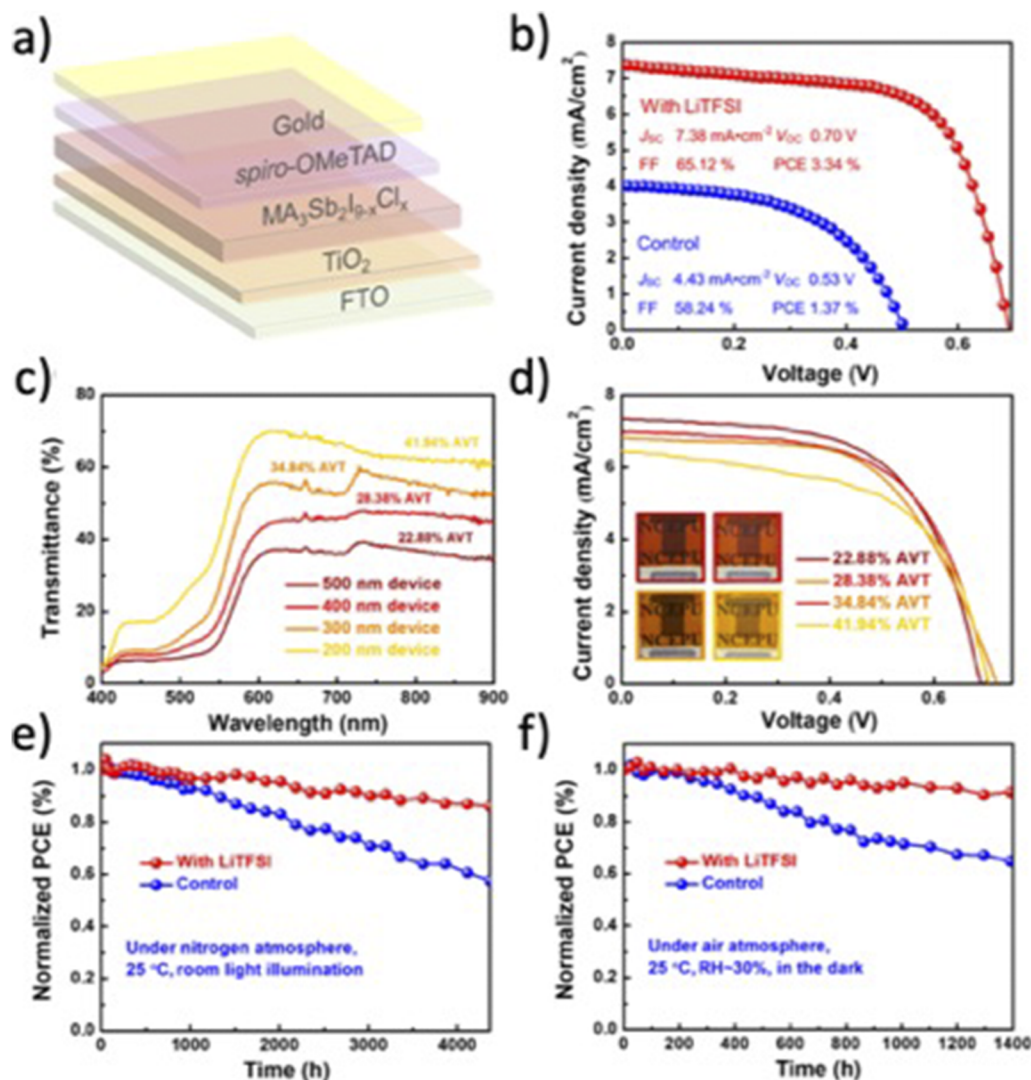


FIG. 18. LiTFSI addition to MA₃Sb₂I_{9-x}Cl_x PIM and OPV stability tests. Adapted with permission from Yang *et al.*, ACS Appl. Mater. Interfaces **12**(14), 17062–17069 (2020). Copyright 2020 American Chemical Society.

Lewis base and as a complimentary ETL for an antimony-based PIM to improve both the quality and the spectral coverage of the light-absorber film. The resulting solar cells (with the architecture ITO/PEDOT:PSS/Cs₃Sb₂I₉/ITIC/PCBM/Ca) showed the highest reported efficiency so far, to the best of our knowledge, i.e., 3.25%.

The compositional manipulation of Cs₃Sb₂I₉ to realize a reproducible 0D to 2D structural conversion, while preventing the formation of the preferential in-plane orientation, commonly obtained by solution-based low-temperature routes involving a mixture of halides (chloride and iodide), is a relevant result reported in a recent study of Peng *et al.*¹⁰¹ In this contribution, the active layer is composed of a sandwich structure (Cs₃Sb₂Cl₃I₆/Cs₃Sb₂I₉) that allows obtaining unoriented perovskite films that provide superior EQEs. The consequence of this outcome is that layered all-inorganic Sb

halides could potentially deliver higher PV performances by aligning their perovskite sheets in the out-of-plane direction as it usually occurs in layered LHPs.¹⁶¹

VI. CONCLUSIONS

In this Review, we combine discussion on theoretical background and experimental results to provide an up-to-date overview of the potential for application in IPV of three representative PIMs, which are the DP Cs₂AgBiBr₆, here considered as a model system for pnictogens-based species, BiOI, and Cs₃Sb₂I_{9-x}Cl_x. Although the current (I)PV performance of these semiconductors is still rather low (PCEs rarely above 5%), their bandgaps (in particular

the ones of the two latter PIMs) are close to the optimum value of 1.9 eV, with EQE spectra in devices matching very well the emission spectra of WLEDs and FLs. Ideal IPV cell efficiencies have been estimated to have the potential to reach maximum values around 40% (but only slightly more than 10% for the Ag–Bi DP).⁶ Those numbers justify the need for more thorough investigations to be carried out in the future on performance optimization in these materials, which will be achieved through a better understanding of their defects physics as well as their structural and morphological arrangements when deposited as thin films. For example, in this Review, we described how doping of such materials can on the one hand tune the bandgap toward optimum values and on the other also improve properties such as carrier mobility and lifetime, i.e., for hydrogenated $\text{Cs}_2\text{AgBiBr}_6$.⁶⁰ Therefore, we believe that further research on this process will improve the efficiency of PIMs as indoor light-harvesters, eventually.

However, this cannot be seen as the only advantage to investigate the implementation of BiOI and $\text{Cs}_3\text{Sb}_2\text{I}_{9-x}\text{Cl}_x$ in light energy harvesting devices. Perhaps, the biggest advantage is deriving from the good level of sustainability characteristics of these PIMs, based on low-toxicity elements like the heaviest pnictogens Sb and Bi, which contrasts with that of other emerging semiconductors of the same family, i.e., the LHPs. The purchase criticality of the former compared to the latter is currently more pronounced, but there are very optimistic perspectives for an increased recycling rate, which will certainly be sought if demonstration for technological and, consequently, industrial utility is achieved. In the end, silicon, the main protagonist of the semiconductor industry, is also listed among CRMs, but this does not prevent its widespread implementation in a wide range of applications for which semiconductors are necessary.

The current requirements for more sustainable energy harvesters, which can also be produced at low costs and undergo ease of recovery *postmortem*, calls for a collective effort involving materials scientists, physicists, and engineers toward the identification of the most promising semiconductors, taking into consideration the many aspects discussed above. We believe that for the two emerging PIMs discussed here, by taking inspiration from what has been previously learned for the more studied $\text{Cs}_2\text{AgBiBr}_6$, it will be possible to achieve excellent results in terms of device efficiency within the next 5–10 years, whereas the environmental stability is already a well-recognized asset. In this way, we soon expect to have IPV devices to power our IoT systems within households and other private or public spaces and also perhaps within “delicate” environments, such as those connected to agriculture and farming, based on these and other similar materials, which will contribute to close the loop between energy efficiency and sustainability of production and operation.

ACKNOWLEDGMENTS

T.G. would like to acknowledge the financial support provided by the European Commission through the H2020 FET-PROACTIVE-EIC-07-2020 project LIGHT-CAP (Grant No. G.A. 101017821), by the European Research Council through the ERC StG project JANUS BI (Grant No. G.A. 101041229), and by the Deutsche Forschungsgemeinschaft (DFG, German Research

Foundation) through the project Grant No. GA 3052/1-1. T.G. acknowledges the support of the Justus Liebig University Giessen through the Herbert-Stolzenberg-Preis for research 2022.

AUTHOR DECLARATIONS

Conflict of Interest

The authors have no conflicts to disclose.

Author Contributions

Fabian Schmitz: Conceptualization (lead); Data curation (equal); Formal analysis (equal); Funding acquisition (lead); Investigation (equal); Methodology (equal); Project administration (equal); Resources (lead); Supervision (equal); Validation (equal); Writing – original draft (equal); Writing – review & editing (equal). **Ribhu Bhatia:** Data curation (equal); Formal analysis (equal); Investigation (equal); Methodology (equal); Project administration (equal); Writing – original draft (equal); Writing – review & editing (equal). **Francesco Lamberti:** Data curation (equal); Formal analysis (equal); Investigation (equal); Methodology (equal); Project administration (equal); Writing – original draft (equal); Writing – review & editing (equal). **Simone Meloni:** Conceptualization (lead); Data curation (equal); Formal analysis (equal); Funding acquisition (lead); Investigation (equal); Methodology (equal); Project administration (lead); Resources (lead); Supervision (equal); Validation (equal); Writing – original draft (equal); Writing – review & editing (equal). **Teresa Gatti:** Conceptualization (lead); Funding acquisition (lead); Investigation (equal); Methodology (equal); Project administration (lead); Resources (lead); Supervision (equal); Validation (equal); Writing – original draft (equal); Writing – review & editing (equal).

DATA AVAILABILITY

Data sharing is not applicable to this article as no new data were created or analyzed in this study.

REFERENCES

- S. Zeadally and O. Bello, “Harnessing the power of internet of things based connectivity to improve healthcare,” *Internet Things* **14**, 100074 (2021).
- X. Gao, P. Pishdad-Bozorgi, D. R. Shelden, and S. Tang, “Internet of things enabled data acquisition framework for smart building applications,” *J. Constr. Eng. Manage.* **147**(2), 04020169 (2021).
- H. Pei Breivold, “Towards factories of the future: Migration of industrial legacy automation systems in the cloud computing and internet-of-things context,” *Enterp. Inf. Syst.* **14**(4), 542–562 (2020).
- E. Twahirwa, J. Rwigema, and R. Datta, “Design and deployment of vehicular internet of things for smart city applications,” *Sustainability* **14**(1), 176 (2021).
- D. P. Abreu, K. Velasquez, M. Curado, and E. Monteiro, “A resilient internet of things architecture for smart cities,” *Ann. Telecommun.* **72**(1–2), 19–30 (2017).
- V. Pecunia, L. G. Occhipinti, and R. L. Z. Hoye, “Emerging indoor photovoltaic technologies for sustainable internet of things,” *Adv. Energy Mater.* **11**(29), 2100698 (2021).
- S. Rühle, “Tabulated values of the Shockley-Queisser limit for single junction solar cells,” *Sol. Energy* **130**, 139–147 (2016).
- M. J. Wu, C. C. Kuo, L. S. Jhuang, P. H. Chen, Y. F. Lai, and F. C. Chen, “Bandgap engineering enhances the performance of mixed-cation perovskite materials for indoor photovoltaic applications,” *Adv. Energy Mater.* **9**(37), 1901863 (2019).

- ⁹J. K. W. Ho, H. Yin, and S. K. So, "From 33% to 57%—An elevated potential of efficiency limit for indoor photovoltaics," *J. Mater. Chem. A* **8**(4), 1717–1723 (2020).
- ¹⁰G. Jarosz, R. Marczyński, and R. Signerski, "Effect of band gap on power conversion efficiency of single-junction semiconductor photovoltaic cells under white light phosphor-based LED illumination," *Mater. Sci. Semicond. Process.* **107**, 104812 (2020).
- ¹¹A. Saha, K. A. Haque, and M. Z. Baten, "Performance evaluation of single-junction indoor photovoltaic devices for different absorber bandgaps under spectrally varying white light-emitting diodes," *IEEE J. Photovoltaics* **10**(2), 539–545 (2020).
- ¹²H. K. H. Lee, Z. Li, J. R. Durrant, and W. C. Tsoi, "Is organic photovoltaics promising for indoor applications?," *Appl. Phys. Lett.* **108**(25), 253301 (2016).
- ¹³B. Li, B. Hou, and G. A. J. Amaratunga, "Indoor photovoltaics, the next big trend in solution-processed solar cells," *InfoMat* **3**(5), 445–459 (2021).
- ¹⁴N. H. Reich, W. G. J. H. M. van Sark, and W. C. Turkenburg, "Charge yield potential of indoor-operated solar cells incorporated into product integrated photovoltaic (PIPV)," *Renewable Energy* **36**(2), 642–647 (2011).
- ¹⁵M. Freunek, M. Freunek, and L. M. Reindl, "Maximum efficiencies of indoor photovoltaic devices," *IEEE J. Photovoltaics* **3**(1), 59–64 (2013).
- ¹⁶C. Wehrenfennig, G. E. Eperon, M. B. Johnston, H. J. Snaith, and L. M. Herz, "High charge carrier mobilities and lifetimes in organolead trihalide perovskites," *Adv. Mater.* **26**(10), 1584–1589 (2014).
- ¹⁷S. D. Stranks, G. E. Eperon, G. Grancini, C. Menelaou, M. J. P. Alcocer, T. Leijtens, L. M. Herz, A. Petrozza, and H. J. Snaith, "Electron-hole diffusion lengths exceeding 1 micrometer in an organometal trihalide perovskite absorber," *Science* **342**(6156), 341–344 (2013).
- ¹⁸A. Miyata, A. Mitoglu, P. Plochocka, O. Portugall, J. T. W. Wang, S. D. Stranks, H. J. Snaith, and R. J. Nicholas, "Direct measurement of the exciton binding energy and effective masses for charge carriers in organic-inorganic tri-halide perovskites," *Nat. Phys.* **11**(7), 582–587 (2015).
- ¹⁹N.R.E.L. (NREL), Best Research Efficiency, http://www.nrel.gov/ncpv/Images/Efficiency_Chart.jpg, 2016.
- ²⁰L. Protesescu, S. Yakunin, M. I. Bodnarchuk, F. Krieg, R. Caputo, C. H. Hendon, R. X. Yang, A. Walsh, and M. V. Kovalenko, "Nanocrystals of cesium lead halide perovskites (CsPbX₃, X = Cl, Br, and I): Novel optoelectronic materials showing bright emission with wide color gamut," *Nano Lett.* **15**(6), 3692–3696 (2015).
- ²¹V. K. Ravi, G. B. Markad, and A. Nag, "Band edge energies and excitonic transition probabilities of colloidal CsPbX₃ (X = Cl, Br, I) perovskite nanocrystals," *ACS Energy Lett.* **1**(4), 665–671 (2016).
- ²²S. Meloni, G. Palermo, N. Ashari-Astani, M. Grätzel, and U. Rothlisberger, "Valence and conduction band tuning in halide perovskites for solar cell applications," *J. Mater. Chem. A* **4**(41), 15997–16002 (2016).
- ²³M. Wang, Q. Wang, J. Zhao, Y. Xu, H. Wang, X. Zhou, S. Yang, Z. Ci, and Z. Jin, "Low-trap-density CsPbX₃ film for high-efficiency indoor photovoltaics," *ACS Appl. Mater. Interfaces* **14**(9), 11528–11537 (2022).
- ²⁴M. Li, C. Zhao, Z.-K. Wang, C.-C. Zhang, H. K. H. Lee, A. Pockett, J. Barbé, W. C. Tsoi, Y.-G. Yang, M. J. Carnie, X.-Y. Gao, W.-X. Yang, J. R. Durrant, L.-S. Liao, and S. M. Jain, "Interface modification by ionic liquid: A promising candidate for indoor light harvesting and stability improvement of planar perovskite solar cells," *Adv. Energy Mater.* **8**(24), 1801509 (2018).
- ²⁵C. Dong, X.-M. Li, C. Ma, W.-F. Yang, J.-J. Cao, F. Igbari, Z.-K. Wang, and L.-S. Liao, "Lycopene-based bionic membrane for stable perovskite photovoltaics," *Adv. Funct. Mater.* **31**(25), 2011242 (2021).
- ²⁶R. Cheng, C.-C. Chung, H. Zhang, F. Liu, W.-T. Wang, Z. Zhou, S. Wang, and A. B. Djurišić, "Tailoring triple-anion perovskite material for indoor light harvesting with restrained halide segregation and record high efficiency beyond 36%," *Adv. Energy Mater.* **9**(38), 1901980 (2019).
- ²⁷X. He, J. Chen, X. Ren, L. Zhang, Y. Liu, J. Feng, J. Fang, K. Zhao, and S. F. Liu, "40.1% record low-light solar-cell efficiency by holistic trap-passivation using micrometer-thick perovskite film," *Adv. Mater.* **33**(27), 2100770 (2021).
- ²⁸Z. Saki, M. M. Byrnavand, N. Taghavinia, M. Kedia, and M. Saliba, "Solution-processed perovskite thin-films: The journey from lab- to large-scale solar cells," *Energy Environ. Sci.* **14**(11), 5690–5722 (2021).
- ²⁹Y. Hu, T. Niu, Y. Liu, Y. Zhou, Y. Xia, C. Ran, Z. Wu, L. Song, P. Müller-Buschbaum, Y. Chen, and W. Huang, "Flexible perovskite solar cells with high power-per-weight: Progress, application, and perspectives," *ACS Energy Lett.* **6**(8), 2917–2943 (2021).
- ³⁰K. Wojciechowski and D. Forgács, "Commercial applications of indoor photovoltaics based on flexible perovskite solar cells," *ACS Energy Lett.* **7**(10), 3729–3733 (2022).
- ³¹K. O. Brinkmann, J. Zhao, N. Pourdavoud, T. Becker, T. Hu, S. Olthof, K. Meerholz, L. Hoffmann, T. Gahlmann, R. Heiderhoff, M. F. Oszejka, N. A. Luechinger, D. Rogalla, Y. Chen, B. Cheng, and T. Riedl, "Suppressed decomposition of organometal halide perovskites by impermeable electron-extraction layers in inverted solar cells," *Nat. Commun.* **8**, 13938 (2017).
- ³²D. Zhang, D. Li, Y. Hu, A. Mei, and H. Han, "Degradation pathways in perovskite solar cells and how to meet international standards," *Commun. Mater.* **3**, 58 (2022).
- ³³D. Di Girolamo, M. I. Dar, D. Dini, L. Gontrani, R. Caminiti, A. Mattoni, M. Graetzel, S. Meloni, and S. Meloni, "Dual effect of humidity on cesium lead bromide: Enhancement and degradation of perovskite films," *J. Mater. Chem. A* **7**(19), 12292–12302 (2019).
- ³⁴B. Li and W. Zhang, "Improving the stability of inverted perovskite solar cells towards commercialization," *Commun. Mater.* **3**, 65 (2022).
- ³⁵C.-H. Chen, S.-N. Cheng, L. Cheng, and Z.-K. Wang, "Toxicity, leakage, and recycling of lead in perovskite photovoltaics," *Adv. Energy Mater.* **13**, 2204144 (2023).
- ³⁶A. H. Slavney, T. Hu, A. M. Lindenberg, and H. I. Karunadasa, "A bismuth-halide double perovskite with long carrier recombination lifetime for photovoltaic applications," *J. Am. Chem. Soc.* **138**(7), 2138–2141 (2016).
- ³⁷Y. Peng, T. N. Huq, J. Mei, L. Portilla, R. A. Jagt, L. G. Occhipinti, J. L. MacManus-Driscoll, R. L. Z. Hoyer, and V. Pecunia, "Lead-free perovskite-inspired absorbers for indoor photovoltaics," *Adv. Energy Mater.* **11**(1), 2002761 (2021).
- ³⁸S. T. Thornton, G. Abdelmageed, R. F. Kahwagi, and G. I. Koleilat, "Progress towards lead-free, efficient, and stable perovskite solar cells," *J. Chem. Technol. Biotechnol.* **97**(4), 810–829 (2022).
- ³⁹W.-F. Yang, J.-J. Cao, C. Dong, M. Li, Q. S. Tian, Z. K. Wang, and L. S. Liao, "Suppressed oxidation of tin perovskite by Catechin for eco-friendly indoor photovoltaics," *Appl. Phys. Lett.* **118**(2), 023501 (2021).
- ⁴⁰J. Cao, Y.-H. Lou, W.-F. Yang, K.-L. Wang, Z.-H. Su, J. Chen, C.-H. Chen, C. Dong, X.-Y. Gao, and Z.-K. Wang, "Multifunctional potassium thiocyanate interlayer for eco-friendly tin perovskite indoor and outdoor photovoltaics," *Chem. Eng. J.* **433**(3), 133832 (2022).
- ⁴¹R. E. Brandt, J. R. Poindexter, P. Gorai, R. C. Kurchin, R. L. Z. Hoyer, L. Nienhaus, M. W. B. Wilson, J. A. Polizzotti, R. Sereika, R. Žaltauskas, L. C. Lee, J. L. Macmanus-Driscoll, M. Bawendi, V. Stevanović, and T. Buonassisi, "Searching for 'defect-tolerant' photovoltaic materials: Combined theoretical and experimental screening," *Chem. Mater.* **29**(11), 4667–4674 (2017).
- ⁴²Y. M. Lee, I. Maeng, J. Park, M. Song, J. H. Yun, M. C. Jung, and M. Nakamura, "Comprehensive understanding and controlling the defect structures: An effective approach for organic-inorganic hybrid perovskite-based solar-cell application," *Front. Energy Res.* **6**, 128 (2018).
- ⁴³A. M. Ganose, D. O. Scanlon, A. Walsh, and R. L. Z. Hoyer, "The defect challenge of wide-bandgap semiconductors for photovoltaics and beyond," *Nat. Commun.* **13**(1), 4715 (2022).
- ⁴⁴W. J. Yin, T. Shi, and Y. Yan, "Unusual defect physics in CH₃NH₃PbI₃ perovskite solar cell absorber," *Appl. Phys. Lett.* **104**(6), 063903 (2014).
- ⁴⁵C. Y. Chen, J. H. Chang, K. M. Chiang, H. L. Lin, S. Y. Hsiao, and H. W. Lin, "Perovskite photovoltaics for dim-light applications," *Adv. Funct. Mater.* **25**(45), 7064–7070 (2015).
- ⁴⁶C. Borbinha, F. Serrazina, M. Salavisa, and M. Viana-Baptista, "Bismuth encephalopathy—A rare complication of long-standing use of bismuth subsalicylate," *BMC Neurol.* **19**(1), 212 (2019).
- ⁴⁷P. T. Reynolds, K. C. Abalos, J. Hopp, and M. E. Williams, "Bismuth toxicity: A rare cause of neurologic dysfunction," *Int. J. Clin. Med.* **3**(1), 46–48 (2012).
- ⁴⁸M. F. Gordon, R. I. Abrams, D. B. Rubin, W. B. Barr, and D. D. Correa, "Bismuth subsalicylate toxicity as a cause of prolonged encephalopathy with myoclonus," *Mov. Disord.* **10**(2), 220–222 (1995).
- ⁴⁹R. Wang, H. Li, and H. Sun, "Bismuth: Environmental pollution and health effects," in *Encyclopedia of Environmental Health* (Elsevier, 2019), pp. 415–423.

- ⁵⁰S. Sundar and J. Chakravarty, "Antimony toxicity," *Int. J. Environ. Res. Public Health* **7**(12), 4267–4277 (2010).
- ⁵¹C. J. Boreiko and T. G. Rossman, "Antimony and its compounds: Health impacts related to pulmonary toxicity, cancer, and genotoxicity," *Toxicol. Appl. Pharmacol.* **403**, 115156 (2020).
- ⁵²A. Periferakis, A. Caruntu, A. T. Periferakis, A. E. Scheau, I. A. Badarau, C. Caruntu, and C. Scheau, "Availability, toxicology and medical significance of antimony," *Int. J. Environ. Res. Public Health* **19**(8), 4669 (2022).
- ⁵³T. Henckens, "Scarce mineral resources: Extraction, consumption and limits of sustainability," *Resour., Conserv. Recycl.* **169**, 105511 (2021).
- ⁵⁴G. Schileo and G. Grancini, "Lead or no lead? Availability, toxicity, sustainability and environmental impact of lead-free perovskite solar cells," *J. Mater. Chem. C* **9**(1), 67–76 (2021).
- ⁵⁵T. Gatti, F. Lamberti, R. Mazzaro, I. Kriegl, D. Schlettwein, F. Enrichi, N. Lago, E. Di Maria, G. Meneghesso, A. Vomiero, and S. Gross, "Opportunities from doping of non-critical metal oxides in last generation light-conversion devices," *Adv. Energy Mater.* **11**(31), 2101041 (2021).
- ⁵⁶E. Deady, C. Moon, K. Moore, K. M. Goodenough, and R. K. Shail, "Bismuth: Economic geology and value chains," *Ore Geol. Rev.* **143**, 104722 (2022).
- ⁵⁷A. Babayigit, A. Ethirajan, M. Muller, and B. Conings, "Toxicity of organometal halide perovskite solar cells," *Nat. Mater.* **15**(3), 247–251 (2016).
- ⁵⁸F. Ünlü, M. Deo, S. Mathur, T. Kirchartz, and A. Kulkarni, "Bismuth-based halide perovskite and perovskite-inspired light absorbing materials for photovoltaics," *J. Phys. D: Appl. Phys.* **55**(11), 113002 (2022).
- ⁵⁹Y. T. Huang, S. R. Kavanagh, D. O. Scanlon, A. Walsh, and R. L. Z. Hoyer, "Perovskite-inspired materials for photovoltaics and beyond-from design to devices," *Nanotechnology* **32**(13), 132004 (2021).
- ⁶⁰Z. Zhang, Q. Sun, Y. Lu, F. Lu, X. Mu, S.-H. Wei, and M. Sui, "Hydrogenated $\text{Cs}_2\text{AgBiBr}_6$ for significantly improved efficiency of lead-free inorganic double perovskite solar cell," *Nat. Commun.* **13**(1), 3397 (2022).
- ⁶¹T. I. Alanazi, "Design and device numerical analysis of lead-free $\text{Cs}_2\text{AgBiBr}_6$ double perovskite solar cell," *Crystals* **13**(2), 267 (2023).
- ⁶²W. Ning, J. Bao, Y. Puttison, F. Moro, L. Kobera, S. Shimono, L. Wang, F. Ji, M. Cuartero, S. Kawaguchi, S. Abbreht, H. Ishibashi, R. de Marco, I. A. Bouianova, G. A. Crespo, Y. Kubota, J. Brus, D. Y. Chung, L. Sun, W. M. Chen, M. G. Kanatzidis, and F. Gao, "Magnetizing lead-free halide double perovskites," *Sci. Adv.* **6**(45), eabb5381 (2020).
- ⁶³G. Feng, Y. Qin, C. Ran, L. Ji, L. Dong, and W. Li, "Structural evolution and photoluminescence properties of a 2D hybrid perovskite under pressure," *APL Mater.* **6**(11), 114201 (2018).
- ⁶⁴H. Lei, D. Hardy, and F. Gao, "Lead-free double perovskite $\text{Cs}_2\text{AgBiBr}_6$: Fundamentals, applications, and perspectives," *Adv. Funct. Mater.* **31**(49), 2105898 (2021).
- ⁶⁵X. G. Zhao, J. H. Yang, Y. Fu, D. Yang, Q. Xu, L. Yu, S. H. Wei, and L. Zhang, "Design of lead-free inorganic halide perovskites for solar cells via cation-transmutation," *J. Am. Chem. Soc.* **139**(7), 2630–2638 (2017).
- ⁶⁶E. T. McClure, M. R. Ball, W. Windl, and P. M. Woodward, " $\text{Cs}_2\text{AgBiX}_6$ (X = Br, Cl): New visible light absorbing, lead-free halide perovskite semiconductors," *Chem. Mater.* **28**(5), 1348–1354 (2016).
- ⁶⁷M. R. Filip, S. Hillman, A. A. Haghighirad, H. J. Snaith, and F. Giustino, "Band gaps of the lead-free halide double perovskites $\text{Cs}_2\text{BiAgCl}_6$ and $\text{Cs}_2\text{BiAgBr}_6$ from theory and experiment," *J. Phys. Chem. Lett.* **7**(13), 2579–2585 (2016).
- ⁶⁸J. Yang, P. Zhang, and S.-H. Wei, "Band structure engineering of $\text{Cs}_2\text{AgBiBr}_6$ perovskite through order-disordered transition: A first-principle study," *J. Phys. Chem. Lett.* **9**, 31–35 (2018).
- ⁶⁹R. Fu, Y. Chen, X. Yong, Z. Ma, L. Wang, P. Lv, S. Lu, G. Xiao, and B. Zou, "Pressure-induced structural transition and band gap evolution of double perovskite $\text{Cs}_2\text{AgBiBr}_6$ nanocrystals," *Nanoscale* **11**(36), 17004–17009 (2019).
- ⁷⁰M. N. Islam, J. Podder, T. Saha, and P. Rani, "Semiconductor to metallic transition under induced pressure in $\text{Cs}_2\text{AgBiBr}_6$ double halide perovskite: A theoretical DFT study for photovoltaic and optoelectronic applications," *RSC Adv.* **11**(39), 24001–24012 (2021).
- ⁷¹W. A. C. Pamodani Wanniarachchi, H. Eidsvag, T. Arunasalam, P. Ravirajan, D. Velauthapillai, and P. Vajeeston, " $\text{Cs}_2\text{AgBiBr}_6$ as a mixed anion perovskites for photovoltaic applications: A first-principle study," *Mater. Today: Proc.* **64**(5), 1783–1788 (2022).
- ⁷²D. Han, T. Zhang, M. Huang, D. Sun, M. H. Du, and S. Chen, "Predicting the thermodynamic stability of double-perovskite halides from density functional theory," *APL Mater.* **6**(8), 084902 (2018).
- ⁷³Z. Li, S. R. Kavanagh, M. Napari, R. G. Palgrave, M. Abdi-Jalebi, Z. Andaji-Garmaroudi, D. W. Davies, M. Laitinen, J. Julin, M. A. Isaacs, R. H. Friend, D. O. Scanlon, A. Walsh, and R. L. Z. Hoyer, "Bandgap lowering in mixed alloys of $\text{Cs}_2\text{Ag}(\text{Sb}_x\text{Bi}_{1-x})\text{Br}_6$ double perovskite thin films," *J. Mater. Chem. A* **8**(41), 21780–21788 (2020).
- ⁷⁴W. Tress and M. T. Sirtl, " $\text{Cs}_2\text{AgBiBr}_6$ double perovskites as lead-free alternatives for perovskite solar cells?," *Sol. RRL* **6**(2), 2100770 (2022).
- ⁷⁵L. Yu and A. Zunger, "Identification of potential photovoltaic absorbers based on first-principles spectroscopic screening of materials," *Phys. Rev. Lett.* **108**(6), 068701 (2012).
- ⁷⁶Y. Bekenstein, J. C. Dahl, J. Huang, W. T. Osowiecki, J. K. Swabeck, E. M. Chan, P. Yang, and A. P. Alivisatos, "The making and breaking of lead-free double perovskite nanocrystals of cesium silver-bismuth halide compositions," *Nano Lett.* **18**(6), 3502–3508 (2018).
- ⁷⁷R. L. Z. Hoyer, L. Eyre, F. Wei, F. Brivio, A. Sadhanala, S. Sun, W. Li, K. H. L. Zhang, J. L. MacManus-Driscoll, P. D. Bristowe, R. H. Friend, A. K. Cheetham, and F. Deschler, "Fundamental carrier lifetime exceeding 1 μs in $\text{Cs}_2\text{AgBiBr}_6$ double perovskite," *Adv. Mater. Interfaces* **5**(15), 1800464 (2018).
- ⁷⁸S. J. Zelewski, J. M. Urban, A. Surrente, D. K. Maude, A. Kuc, L. Schade, R. D. Johnson, M. Dollmann, P. K. Nayak, H. J. Snaith, P. Radaelli, R. Kudrawiec, R. J. Nicholas, P. Plochocka, and M. Baranowski, "Revealing the nature of photoluminescence emission in the metal-halide double perovskite $\text{Cs}_2\text{AgBiBr}_6$," *J. Mater. Chem. C* **7**(27), 8350–8356 (2019).
- ⁷⁹B. Wu, W. Ning, Q. Xu, M. Manjappa, M. Feng, S. Ye, J. Fu, S. Lie, T. Yin, F. Wang, T. W. Goh, P. C. Harikeesh, Y. K. E. Tay, Z. X. Shen, F. Huang, R. Singh, G. Zhou, F. Gao, and T. Chien Sum, "Strong self-trapping by deformation potential limits photovoltaic performance in bismuth double perovskite," *Sci. Adv.* **7**(8), eabd3160 (2021).
- ⁸⁰Z. Xiao, W. Meng, J. Wang, and Y. Yan, "Thermodynamic stability and defect chemistry of bismuth-based lead-free double perovskites," *ChemSusChem* **9**(18), 2628–2633 (2016).
- ⁸¹T. Handa, T. Yamada, M. Nagai, and Y. Kanemitsu, "Phonon, thermal, and thermo-optical properties of halide perovskites," *Phys. Chem. Chem. Phys.* **22**(45), 26069–26087 (2020).
- ⁸²N. Phung, A. Mattoni, J. A. Smith, D. Skroblin, H. Köbler, L. Choubrac, J. Bernetz, J. Li, T. Unold, S. Schorr, C. Gollwitzer, I. G. Scheblykin, E. L. Unger, M. Saliba, S. Meloni, A. Abate, and A. Merdasa, "Photoprotection in metal halide perovskites by ionic defect formation," *Joule* **6**(9), 2152–2174 (2022).
- ⁸³A. D. Wright, L. R. V. Buizza, K. J. Savill, G. Longo, H. J. Snaith, M. B. Johnston, and L. M. Herz, "Ultrafast excited-state localization in $\text{Cs}_2\text{AgBiBr}_6$ double perovskite," *J. Phys. Chem. Lett.* **12**(13), 3352–3360 (2021).
- ⁸⁴R. L. Z. Hoyer, J. Hidalgo, R. A. Jagt, J. Correa-Baena, T. Fix, and J. L. MacManus-Driscoll, "The role of dimensionality on the optoelectronic properties of oxide and halide perovskites, and their halide derivatives," *Adv. Energy Mater.* **12**(4), 2100499 (2022).
- ⁸⁵M. Sendner, P. K. Nayak, D. A. Egger, S. Beck, C. Müller, B. Epding, W. Kowalsky, L. Kronik, H. J. Snaith, A. Pucci, and R. Lovrincic, "Optical phonons in methylammonium lead halide perovskites and implications for charge transport," *Mater. Horiz.* **3**(6), 613–620 (2016).
- ⁸⁶J. A. Steele, P. Puech, M. Keshavarz, R. Yang, S. Banerjee, E. Debroye, C. W. Kim, H. Yuan, N. H. Heo, J. Vanacke, A. Walsh, J. Hofkens, and M. B. J. Roeffaers, "Giant electron-phonon coupling and deep conduction band resonance in metal halide double perovskite," *ACS Nano* **12**(8), 8081–8090 (2018).
- ⁸⁷K. Miyata, D. Meggiolaro, M. T. Trinh, P. P. Joshi, E. Mosconi, S. C. Jones, F. De Angelis, and X. Zhu, "Large polarons in lead halide perovskites," *Sci. Adv.* **3**(8), e1701217 (2017).
- ⁸⁸H. Sumi and Y. Toyozawa, "Urbach-martensen rule and exciton trapped momentarily by lattice vibrations," *J. Phys. Soc. Jpn.* **31**(2), 342–358 (1971).
- ⁸⁹Y. Toyozawa, "Self-trapping of an electron by the acoustical mode of lattice vibration. I," *Prog. Theor. Phys.* **26**(1), 29–44 (1961).
- ⁹⁰J. Kang and L. W. Wang, "High defect tolerance in lead halide perovskite CsPbBr_3 ," *J. Phys. Chem. Lett.* **8**(2), 489–493 (2017).

- ⁹¹T. Li, X. Zhao, D. Yang, M. Du, and L. Zhang, "Intrinsic defect properties in halide double perovskites for optoelectronic," *Phys. Rev. Appl.* **10**(1), 041001 (2018).
- ⁹²D. Liu, C. M. Perez, A. S. Vasenko, and O. V. Prezhdo, "Ag–Bi charge redistribution creates deep traps in defective $\text{Cs}_2\text{AgBiBr}_6$: Machine learning analysis of density functional theory," *J. Phys. Chem. Lett.* **13**(16), 3645–3651 (2022).
- ⁹³Y. She, Z. Hou, O. V. Prezhdo, and W. Li, "Identifying and passivating killer defects in Pb-free double $\text{Cs}_2\text{AgBiBr}_6$ perovskite," *J. Phys. Chem. Lett.* **12**(43), 10581–10588 (2021).
- ⁹⁴J. Park, J. Calbo, Y. K. Jung, L. D. Whalley, and A. Walsh, "Accumulation of deep traps at grain boundaries in halide perovskites," *ACS Energy Lett.* **4**(6), 1321–1327 (2019).
- ⁹⁵W.-W. Dai and Z.-Y. Zhao, "Electronic structure and optical properties of BiOI as a photocatalyst driven by visible light," *Catalysts* **6**(9), 133 (2016).
- ⁹⁶W. L. Huang and Q. Zhu, "Electronic structures of relaxed BiOX (X = F, Cl, Br, I) photocatalysts," *Comput. Mater. Sci.* **43**(4), 1101–1108 (2008).
- ⁹⁷R. L. Z. Hoyer, L. C. Lee, R. C. Kurchin, T. N. Huq, K. H. L. Zhang, M. Sponceller, L. Nienhaus, R. E. Brandt, J. Jean, J. A. Polizzotti, A. Kursumović, M. G. Bawendi, V. Bulović, V. Stevanović, T. Buonassisi, and J. L. MacManus-Driscoll, "Strongly enhanced photovoltaic performance and defect physics of air-stable bismuth oxyiodide (BiOI)," *Adv. Mater.* **29**(36), 1702176 (2017).
- ⁹⁸T. N. Huq, L. C. Lee, L. Eyre, W. Li, R. A. Jagt, C. Kim, S. Fearn, V. Pecunia, F. Deschler, J. L. Macmanus-driscoll, and R. L. Z. Hoyer, "Electronic structure and optoelectronic properties of bismuth oxyiodide robust against percent-level iodine-, oxygen-, and bismuth-related surface defects," *Adv. Funct. Mater.* **30**(13), 1909983 (2020).
- ⁹⁹M. L. Agiorgousis, Y. Sun, H. Zeng, and S. Zhang, "Strong covalency-induced recombination centers in perovskite solar cell material $\text{CH}_3\text{NH}_3\text{PbI}_3$," *J. Am. Chem. Soc.* **136**(41), 14570–14575 (2014).
- ¹⁰⁰M. Yavari, F. Ebadi, S. Meloni, S. Wang, T. C. Yang, S. Sun, H. Schwartz, Z. Wang, B. Niesen, J. Durantini, P. Rieder, K. Tvingstedt, T. Buonassisi, W. C. H. Choy, A. Filippetti, T. Dittrich, S. Olthof, J.-P. Correa-Baena, and W. Tress, "How far does the defect tolerance of lead-halide perovskites range? The example of Bi impurities introducing efficient recombination centers," *J. Mater. Chem. A* **7**(41), 23838–23853 (2019).
- ¹⁰¹Y. Peng, F. Li, Y. Wang, Y. Li, R. L. Z. Hoyer, L. Feng, K. Xia, and V. Pecunia, "Enhanced photoconversion efficiency in cesium-antimony-halide perovskite derivatives by tuning crystallographic dimensionality," *Appl. Mater. Today* **19**, 100637 (2020).
- ¹⁰²R. Nie, R. R. Sumukam, S. H. Reddy, M. Banavoth, and S. I. Seok, "Lead-free perovskite solar cells enabled by hetero-valent substitutes," *Energy Environ. Sci.* **13**(8), 2363–2385 (2020).
- ¹⁰³J. Mei, M. Liu, P. Vivo, and V. Pecunia, "Two-dimensional antimony-based perovskite-inspired materials for high-performance self-powered photodetectors," *Adv. Funct. Mater.* **31**(50), 2106295 (2021).
- ¹⁰⁴B. Saparov, F. Hong, J.-P. Sun, H.-S. Duan, W. Meng, S. Cameron, I. G. Hill, Y. Yan, and D. B. Mitzi, "Thin-film preparation and characterization of $\text{Cs}_3\text{Sb}_2\text{I}_9$: A lead-free layered perovskite semiconductor," *Chem. Mater.* **27**(16), 5622–5632 (2015).
- ¹⁰⁵C. M. M. Soe, G. P. Nagabhushana, R. Shivaramaiah, H. Tsai, W. Nie, J. C. Blancon, F. Melkonyan, D. H. Cao, B. Traoré, L. Pedesseau, M. Kepenekian, C. Katan, J. Even, T. J. Marks, A. Navrotsky, A. D. Mohite, C. C. Stoumpos, and M. G. Kanatzidis, "Structural and thermodynamic limits of layer thickness in 2D halide perovskites," *Proc. Natl. Acad. Sci. U. S. A.* **116**(1), 58–66 (2019).
- ¹⁰⁶L. Zhang and W. Liang, "How the structures and properties of two-dimensional layered perovskites MAPbI_3 and CsPbI_3 vary with the number of layers," *J. Phys. Chem. Lett.* **8**(7), 1517–1523 (2017).
- ¹⁰⁷T. D. Chonamada, A. B. Dey, and P. K. Santra, "Degradation studies of $\text{Cs}_3\text{Sb}_2\text{I}_9$: A lead-free perovskite," *ACS Appl. Energy Mater.* **3**(1), 47–55 (2020).
- ¹⁰⁸A. Singh, K. M. Boopathi, A. Mohapatra, Y. F. Chen, G. Li, and C. W. Chu, "Photovoltaic performance of vapor-assisted solution-processed layer polymorph of $\text{Cs}_3\text{Sb}_2\text{I}_9$," *ACS Appl. Mater. Interfaces* **10**(3), 2566–2573 (2018).
- ¹⁰⁹J.-G. Park and K.-H. Hong, "Dual-site compositional engineering of bismuth-based halide perovskites for stable and efficient lead-free solar cells," *J. Phys. Chem. C* **125**(24), 13138–13145 (2021).
- ¹¹⁰F. Jiang, D. Yang, Y. Jiang, T. Liu, X. Zhao, Y. Ming, B. Luo, F. Qin, J. Fan, H. Han, L. Zhang, and Y. Zhou, "Chlorine-incorporation-induced formation of the layered phase for antimony-based lead-free perovskite solar cells," *J. Am. Chem. Soc.* **140**(3), 1019–1027 (2018).
- ¹¹¹A. Pradhan, M. K. Jena, and S. L. Samal, "Understanding of the band gap transition in $\text{Cs}_3\text{Sb}_2\text{Cl}_{9-x}\text{Br}_x$: Anion site preference-induced structural distortion," *ACS Appl. Energy Mater.* **5**(6), 6952–6961 (2022).
- ¹¹²F. Igbari, R. Wang, Z. K. Wang, X. J. Ma, Q. Wang, K. L. Wang, Y. Zhang, L. S. Liao, and Y. Yang, "Composition stoichiometry of $\text{Cs}_2\text{AgBiBr}_6$ films for highly efficient lead-free perovskite solar cells," *Nano Lett.* **19**(3), 2066–2073 (2019).
- ¹¹³K. Z. Du, W. Meng, X. Wang, Y. Yan, and D. B. Mitzi, "Bandgap engineering of lead-free double perovskite $\text{Cs}_2\text{AgBiBr}_6$ through trivalent metal alloying," *Angew. Chem., Int. Ed.* **56**(28), 8158–8162 (2017).
- ¹¹⁴R. Kentsch, M. Scholz, J. Horn, D. Schlettwein, K. Oum, and T. Lenzer, "Exciton dynamics and electron-phonon coupling affect the photovoltaic performance of the $\text{Cs}_2\text{AgBiBr}_6$ double perovskite," *J. Phys. Chem. C* **122**(45), 25940–25947 (2018).
- ¹¹⁵N. K. Tailor, S. K. Saini, P. Yadav, M. Kumar, and S. Satapathi, "Elucidating polaron dynamics in $\text{Cs}_2\text{AgBiBr}_6$ double perovskite," *J. Phys. Chem. Lett.* **14**(3), 730–736 (2023).
- ¹¹⁶D. Bartesaghi, A. H. Slavney, M. C. Gélvez-Rueda, B. A. Connor, F. C. Grozema, H. I. Karunadasa, and T. J. Savenije, "Charge carrier dynamics in $\text{Cs}_2\text{AgBiBr}_6$ double perovskite," *J. Phys. Chem. C* **122**(9), 4809–4816 (2018).
- ¹¹⁷F. Schmitz, N. Lago, L. Fagiolar, J. Burkhart, A. Cester, A. Polo, M. Prato, G. Meneghesso, S. Gross, F. Bella, F. Lamberti, and T. Gatti, "High open-circuit voltage $\text{Cs}_2\text{AgBiBr}_6$ carbon-based perovskite solar cells via green processing of ultrasonic spray-coated carbon electrodes from waste tire sources," *ChemSusChem* **15**(22), e202201590 (2022).
- ¹¹⁸L. Zhang, Y. Xu, P. Niu, M. Lyu, H. Lu, and J. Zhu, "Regulating film crystallization kinetics with thiourea additive in $\text{Cs}_2\text{AgBiBr}_6$ solar cells," *J. Phys. D: Appl. Phys.* **56**(7), 075501 (2023).
- ¹¹⁹A. Yang, L. Zhang, Y. Xu, Q. Wang, M. Lyu, H. Lu, and J. Zhu, " V_{OC} over 1.2 V for $\text{Cs}_2\text{AgBiBr}_6$ solar cells based on formamidineum acetate additive," *J. Mater. Sci.: Mater. Electron.* **33**(23), 18758–18767 (2022).
- ¹²⁰H. Peng, P. Fan, Z. Zheng, S. Chen, and G. Liang, "Phase-controlled strategy for high-quality single-source vapor-deposited $\text{Cs}_2\text{AgBiBr}_6$ thin films," *ACS Appl. Energy Mater.* **5**(12), 15058–15068 (2022).
- ¹²¹N. Rodkey, S. Kaal, P. Sebastia-luna, Y. A. Birkhölzer, M. Ledinsky, F. Palazon, H. J. Bolink, and M. Morales-Masis, "Pulsed laser deposition of $\text{Cs}_2\text{AgBiBr}_6$: From mechanochemically synthesized powders to dry, single-step deposition," *Chem. Mater.* **33**(18), 7417–7422 (2021).
- ¹²²Z. Li, S. P. Senanayak, L. Dai, G. Kusch, R. Shivanna, Y. Zhang, D. Pradhan, J. Ye, Y. Huang, H. Siringhaus, R. A. Oliver, N. C. Greenham, R. H. Friend, and R. L. Z. Hoyer, "Understanding the role of grain boundaries on charge-carrier and ion transport in $\text{Cs}_2\text{AgBiBr}_6$ thin films," *Adv. Funct. Mater.* **31**(49), 2104981 (2021).
- ¹²³M. Ghasemi, L. Zhang, J. Yun, M. Hao, D. He, P. Chen, Y. Bai, T. Lin, M. Xiao, A. Du, M. Lyu, and L. Wang, "Dual-ion-diffusion induced degradation in lead-free $\text{Cs}_2\text{AgBiBr}_6$ double perovskite solar cells," *Adv. Funct. Mater.* **30**(42), 2002342 (2020).
- ¹²⁴J. Li, X. Meng, Z. Wu, Y. Duan, R. Guo, W. Xiao, Y. Zhang, Y. Li, Y. Shen, W. Zhang, and G. Shao, "Pinning bromide ion with ionic liquid in lead-free $\text{Cs}_2\text{AgBiBr}_6$ double perovskite solar cells," *Adv. Funct. Mater.* **32**(25), 2112991 (2022).
- ¹²⁵M. Abdelsamie, K. Cruse, N. Tamura, G. Ceder, and C. M. Sutter-Fella, "Impact of processing conditions on the film formation of lead-free halide double perovskite $\text{Cs}_2\text{AgBiBr}_6$," *J. Mater. Chem. A* **10**(37), 19868–19880 (2022).
- ¹²⁶J. Duan, Y. Yang, J. Tang, H. Wan, G. Ma, L. Shen, J. Zhang, H. Wang, and H. Zhou, "MAI enhanced electron extraction in all-inorganic $\text{Cs}_2\text{AgBiBr}_6$ perovskite photovoltaics," *Chem. Commun.* **59**(9), 1173–1176 (2023).
- ¹²⁷M. Alla, V. Manjunath, E. Choudhary, M. Samtham, S. Sharma, P. A. Shaikh, M. Rouchdi, and B. Fares, "Evaluating the potential of lead-free non-toxic $\text{Cs}_2\text{BiAgI}_6$ -based double perovskite solar cell," *Phys. Status Solidi A* **220**(2), 2200642 (2023).
- ¹²⁸H. Wu, A. Erbing, M. B. Johansson, J. Wang, C. Kamal, M. Odelius, and E. M. J. Johansson, "Mixed-halide double perovskite $\text{Cs}_2\text{AgBiX}_6$ (X = Br, I) with tunable optical properties via anion exchange," *ChemSusChem* **14**(20), 4507–4515 (2021).

- ¹²⁹C. W. Ahn, J. H. Jo, J. S. Choi, Y. H. Hwang, I. W. Kim, and T. H. Kim, "Heteroanionic lead-free double-perovskite halides for bandgap engineering," *Adv. Eng. Mater.* **25**(1), 2201119 (2023).
- ¹³⁰A. C. Dakshinamurthy, M. Gupta, B. R. K. Nanda, and C. Sudakar, "Anionic alloying in hybrid halide $\text{Cs}_2\text{AgBiBr}_{6-x}\text{Cl}_x$ double perovskites: Is it true alloying or preferential occupation of halide ions in MX_6 octahedra," *J. Phys. Chem. C* **127**(3), 1588–1597 (2023).
- ¹³¹S. Yoon, B. Fett, A. Frebel, S. Kroisl, B. Herbig, M. Widenmeyer, B. Balke, G. Sextl, K. Mandel, and A. Weidenkaff, "Sb-substituted $\text{Cs}_2\text{AgBiBr}_6$ —As much as it could Be?—Influence of synthesis methods on Sb-substitution level in $\text{Cs}_2\text{AgBiBr}_6$," *Energy Technol.* **10**(8), 2200197 (2022).
- ¹³²M. A. Hadi, N. Islam, and J. Podder, "Indirect to direct band gap transition through order to disorder transformation of $\text{Cs}_2\text{AgBiBr}_6$ via creating anti-site defects for optoelectronic and photovoltaic applications," *RSC Adv.* **12**(24), 15461–15469 (2022).
- ¹³³Y. Zhang, Y. Song, Y. Lu, Z. Zhang, Y. Wang, Y. Yang, Q. Dong, Y. Yu, P. Qin, and F. Huang, "Thermochromic $\text{Cs}_2\text{AgBiBr}_6$ single crystal with decreased band gap through order-disorder transition," *Small* **18**(24), 2201943 (2022).
- ¹³⁴A. C. Dakshinamurthy and C. Sudakar, "Photoinduced degradation of thermally stable $\text{Cs}_2\text{AgBiBr}_6$ double perovskites by micro-Raman studies," *Mater. Adv.* **3**(14), 5813–5817 (2022).
- ¹³⁵J. Gebhardt and C. Elsässer, "The electronic structure of $\text{Cs}_2\text{AgBiBr}_6$ at room temperature," *Phys. Status Solidi B* **259**(8), 2200124 (2022).
- ¹³⁶N. K. Tailor, N. Parikh, P. Yadav, and S. Satapathi, "Dielectric relaxation and polaron hopping in $\text{Cs}_2\text{AgBiBr}_6$ halide double perovskites," *J. Phys. Chem. C* **126**(24), 10199–10208 (2022).
- ¹³⁷V. Andrei, R. A. Jagt, M. Rahaman, L. Lari, V. K. Lazarov, J. L. Macmanus-driscoll, R. L. Z. Hoye, and E. Reisner, "Long-term solar water and CO_2 splitting with photoelectrochemical BiOI – BiVO_4 tandems," *Nat. Mater.* **21**, 864–868 (2022).
- ¹³⁸Y. C. Choi and R. Nie, "Heavy pnictogen chalcogenides for efficient, stable, and environmentally friendly solar cell applications," *Nanotechnology* **34**(14), 142001 (2023).
- ¹³⁹A. Crovetto, A. Hajjifarassar, O. Hansen, B. Seger, I. Chorkendorff, and P. C. K. Vesborg, "Parallel evaluation of the BiI_3 , BiOI , and Ag_3BiI_6 layered photoabsorbers," *Chem. Mater.* **32**(8), 3385–3395 (2020).
- ¹⁴⁰R. A. Jagt, T. N. Huq, K. M. Börsig, D. Sauven, L. C. Lee, J. L. Macmanus-driscoll, and R. L. Z. Hoye, "Controlling the preferred orientation of layered BiOI solar absorbers," *J. Mater. Chem. C* **8**(31), 10791–10797 (2020).
- ¹⁴¹A. A. Putri, A. A. Abuelwafa, S. Kato, N. Kishi, and T. Soga, "A simple spin-assisted SILAR of bismuth oxyiodide films preparation for photovoltaic application," *SN Appl. Sci.* **2**(1), 119 (2020).
- ¹⁴²R. M. Matiur, A. A. Abuelwafa, A. A. Putri, S. Kato, N. Kishi, and T. Soga, "Annealing effects on structural and photovoltaic properties of the dip-SILAR-prepared bismuth oxyhalides (BiOI , $\text{Bi}_7\text{O}_9\text{I}_3$, $\text{Bi}_5\text{O}_7\text{I}$) films," *SN Appl. Sci.* **3**(2), 138 (2021).
- ¹⁴³T. Feeney, G. Ayyur, T. Nguyen, S. Farooq, J. Mendes, H. Tuohey, D. E. Gómez, E. Della Gaspera, and J. van Embden, "Solution processed bismuth oxyiodide (BiOI) thin films and solar cells," *Nanotechnology* **34**, 305404 (2023).
- ¹⁴⁴X. Zhang and L. Zhang, "Electronic and band structure tuning of ternary semiconductor photocatalysts by self doping: The case of BiOI ," *J. Phys. Chem. C* **114**(42), 18198–18206 (2010).
- ¹⁴⁵X. Ren, J. Yao, L. Cai, J. Li, X. Cao, Y. Zhang, B. Wang, and Y. Wei, "Band gap engineering of BiOI via oxygen vacancies induced by graphene for improved photocatalysis," *New J. Chem.* **43**(3), 1523–1530 (2019).
- ¹⁴⁶J. Pal, S. Manna, A. Mondal, S. Das, K. V. Adarsh, and A. Nag, "Colloidal synthesis and photophysics of $\text{M}_3\text{Sb}_2\text{I}_9$ ($\text{M} = \text{Cs}$ and Rb) nanocrystals: Lead-free perovskites," *Angew. Chem., Int. Ed.* **56**(45), 14187–14191 (2017).
- ¹⁴⁷A. S. Thomas, "A review on antimony-based perovskite solar cells," *Equilib. J. Chem. Eng.* **6**(2), 75 (2022).
- ¹⁴⁸J.-P. Correa-Baena, L. Nienhaus, R. C. Kurchin, S. S. Shin, S. Wiegold, N. T. Putri Hartono, M. Layurova, N. D. Klein, J. R. Poindexter, A. Polizzotti, S. Sun, M. G. Bawendi, and T. Buonassisi, "A-site cation in inorganic $\text{A}_3\text{Sb}_2\text{I}_9$ perovskite influences structural dimensionality, exciton binding energy, and solar cell performance," *Chem. Mater.* **30**(11), 3734–3742 (2018).
- ¹⁴⁹T. Geng, Z. Ma, Y. Chen, Y. Cao, P. Lv, N. Li, and G. Xiao, "Bandgap engineering in two-dimensional halide perovskite $\text{Cs}_3\text{Sb}_2\text{I}_9$ nanocrystals under pressure," *Nanoscale* **12**(3), 1425–1431 (2020).
- ¹⁵⁰D. Samanta, S. P. Chaudhary, B. Ghosh, S. Bhattacharyya, G. Shukla, and G. D. Mukherjee, "Pressure-induced emission enhancement and bandgap narrowing: Experimental investigations and first-principles theoretical simulations on the model halide perovskite $\text{Cs}_3\text{Sb}_2\text{Br}_9$," *Phys. Rev. B* **105**(10), 104103 (2022).
- ¹⁵¹F. Umar, J. Zhang, Z. Jin, I. Muhammad, X. Yang, H. Deng, K. Jahangeer, Q. Hu, H. Song, and J. Tang, "Dimensionality controlling of $\text{Cs}_3\text{Sb}_2\text{I}_9$ for efficient all-inorganic planar thin film solar cells by HCl-assisted solution method," *Adv. Opt. Mater.* **7**(5), 1801368 (2019).
- ¹⁵²Y. Yang, C. Liu, M. Cai, Y. Liao, Y. Ding, S. Ma, X. Liu, M. Guli, S. Dai, and M. K. Nazeeruddin, "Dimension-controlled growth of antimony-based perovskite-like halides for lead-free and semitransparent photovoltaics," *ACS Appl. Mater. Interfaces* **12**(14), 17062–17069 (2020).
- ¹⁵³I. Wharf, T. Gramstad, R. Makhija, and M. Onyszczuk, "Synthesis and vibrational spectra of some lead(II) halide adducts with O-, S- and N-donor atom ligands," *Can. J. Chem.* **54**(21), 3430–3438 (1976).
- ¹⁵⁴J.-W. Lee, Z. Dai, C. Lee, H. M. Lee, T.-H. Han, N. De Marco, O. Lin, C. S. Choi, B. Dunn, J. Koh, D. Di Carlo, J. H. Ko, H. D. Maynard, and Y. Yang, "Tuning molecular interactions for highly reproducible and efficient formamidinium perovskite solar cells via adduct approach," *J. Am. Chem. Soc.* **140**(20), 6317–6324 (2018).
- ¹⁵⁵N. Ahn, D.-Y. Son, I.-H. Jang, S. M. Kang, M. Choi, and N.-G. Park, "Highly reproducible perovskite solar cells with average efficiency of 18.3% and best efficiency of 19.7% fabricated via Lewis base adduct of lead(II) iodide," *J. Am. Chem. Soc.* **137**(27), 8696–8699 (2015).
- ¹⁵⁶J.-W. Lee, H.-S. Kim, and N.-G. Park, "Lewis acid–base adduct approach for high efficiency perovskite solar cells," *Acc. Chem. Res.* **49**(2), 311–319 (2016).
- ¹⁵⁷A. Singh, S. Najman, A. Mohapatra, Y.-J. Lu, C. Hanmandlu, C.-W. Pao, Y.-F. Chen, C. S. Lai, and C.-W. Chu, "Modulating performance and stability of inorganic lead-free perovskite solar cells via Lewis-pair mediation," *ACS Appl. Mater. Interfaces* **12**(29), 32649–32657 (2020).
- ¹⁵⁸X. Zhao, T. Liu, A. B. Kaplan, C. Yao, and Y.-L. Loo, "Accessing highly oriented two-dimensional perovskite films via solvent-vapor annealing for efficient and stable solar cells," *Nano Lett.* **20**(12), 8880–8889 (2020).
- ¹⁵⁹J. Li, Y. Lv, H. Han, J. Xu, and J. Yao, "Two-dimensional $\text{Cs}_3\text{Sb}_2\text{I}_{9-x}\text{Cl}_x$ film with (201) preferred orientation for efficient perovskite solar cells," *Materials* **15**(8), 2883 (2022).
- ¹⁶⁰A. Singh, P.-T. Lai, A. Mohapatra, C.-Y. Chen, H.-W. Lin, Y.-J. Lu, and C. W. Chu, "Panchromatic heterojunction solar cells for Pb-free all-inorganic antimony based perovskite," *Chem. Eng. J.* **419**, 129424 (2021).
- ¹⁶¹H. Tsai, W. Nie, J.-C. Blancon, C. C. Stoumpos, R. Asadpour, B. Harutyunyan, A. J. Neukirch, R. Verduzco, J. J. Crochet, S. Tretiak, L. Pedesseau, J. Even, M. A. Alam, G. Gupta, J. Lou, P. M. Ajayan, M. J. Bedzyk, M. G. Kanatzidis, and A. D. Mohite, "High-efficiency two-dimensional Ruddlesden–Popper perovskite solar cells," *Nature* **536**(7616), 312–316 (2016).